Architecture of the intact yeast and human rixosomes

Zijie Zheng[1,2,3,5,†], Shu Shu[1,2,3,5], Xiao Li[1,2,3], Shiqi Fan[4], Yuechan Wang[1,2,3], and Huaizong Shen[1,2,3,*,‡]

[1]Zhejiang Key Laboratory of Structural Biology, School of Life Sciences, Westlake University, Hangzhou, Zhejiang, China

[2]Westlake Laboratory of Life Sciences and Biomedicine, Hangzhou, Zhejiang, China

[3]Institute of Biology, Westlake Institute for Advanced Study, Hangzhou, Zhejiang, China

[4]School of Engineering, Westlake University, Hangzhou, Zhejiang, China

[5]These authors contributed equally to this work.

[*]To whom correspondence should be addressed: H. Shen (shenhuaizong@smart.org.cn).

[†]Present address: Department of Biological Sciences, National University of Singapore, Singapore 117558, Singapore

[‡]Present address: Institute of Bio-Architecture and Bio-Interactions (IBABI), Shenzhen Medical Academy of Research and Translation (SMART), Shenzhen 518107, Guangdong, China.

Abstract

The rixosome is an essential, evolutionarily conserved complex that removes internal transcribed spacer 2 (ITS2) during ribosome biogenesis and silences transcription by degrading nascent RNA at heterochromatin. How these two activities are organized within the intact complex is unknown. We report cryo-electron microscopy structures of intact rixosomes purified endogenously from yeast and human cells, and of native rixosome-bound pre-60S intermediates. The yeast holoenzyme comprises a twofold-symmetric Las1$_2$–Grc3$_2$ catalytic core flanked by two Rix1$_2$–Crb3$_2$–Ipi1$_2$ scaffold modules; the human complex adopts the same architecture with a single scaffold. In both species, multivalent interfaces join scaffold to core, and disrupting them impairs ITS2 processing and silencing in vivo. Assembly with the scaffold markedly enhances nuclease and kinase activity relative to the isolated core. On the pre-60S particle, the scaffold anchors adjacent to the ITS2 foot while the catalytic core remains flexibly tethered, and the rixosome stays bound after ITS2 removal, defining the order of ITS2 processing and rixosome release. These results identify the scaffold as the organizational and regulatory hub of the rixosome and provide a framework for interpreting disease-associated rixosome variants.

Introduction

The rixosome is an essential, evolutionarily conserved protein complex that functions in both ribosome biogenesis and chromatin regulation (*1–7*). It catalyzes the endonucleolytic removal of internal transcribed spacer 2 (ITS2) from precursor rRNA during 60S subunit maturation, and it promotes transcriptional silencing by degrading nascent RNA at heterochromatic and Polycomb-regulated loci (*6–10*). In humans, mutations in rixosome subunits cause congenital lethal motor neuron disease and X-linked intellectual disability, underscoring the physiological importance of the complex (*11*, *12*).

The rixosome comprises two modules with distinct functions. The catalytic module is a Las1–Grc3 heterotetramer (LAS1L–NOL9 in humans) in which Las1/LAS1L contributes a HEPN-family endonuclease domain that dimerizes to form a composite active site and Grc3/NOL9 provides a polynucleotide kinase (PNK) domain that phosphorylates the 5′-OH terminus generated by Las1 cleavage (*13–20*). The two enzymes act as a tightly coupled nuclease–kinase unit: Las1 cleavage is strictly Grc3-dependent, and the 5′-phosphate produced by Grc3 is required for subsequent recognition and exonucleolytic trimming by the RNA exosome (*17*, *18*, *21–23*). The scaffold module—Rix1, Crb3, and Ipi1 in yeast (PELP1, WDR18, and TEX10 in humans)—forms an extended platform that tethers the catalytic core and mediates interactions with pre-ribosomal particles and chromatin targets (*6*, *9*, *10*, *24*).

Structural work on the rixosome has so far been limited to isolated subcomplexes and to low-resolution views of the ribosome-associated complex. The Las1–Grc3 nuclease–

kinase module has been characterized biochemically and structurally from several fungal species, revealing the molecular basis of coupled cleavage and phosphorylation (*13*, *14*, *16*, *18*, *20*, *25*), and structures of recombinant human subcomplexes—the PELP1–WDR18–TEX10 scaffold and the LAS1L–NOL9 catalytic module—have been reported in isolation (*9*, *26*, *27*). Cryo-electron microscopy (cryo-EM) studies of pre-60S ribosomal particles have visualized the Rix1-containing scaffold module on assembling ribosomes and have shown how 5S RNP rotation is coordinated with ITS2 processing in fungi (*10*, *28*).

Despite these advances, the structure of the fully assembled holoenzyme at high resolution has remained elusive, and it is unclear how a single complex coordinates two mechanistically distinct activities—pre-rRNA processing and chromatin-associated RNA degradation. Three questions in particular remain open: how the catalytic and scaffold modules are organized within the intact complex and how that organization is coupled to catalytic competence; how ITS2 processing is ordered relative to rixosome release during pre-60S maturation; and whether the architecture of the complex differs between unicellular and multicellular eukaryotes.

Here we present high-resolution cryo-EM structures of intact rixosomes purified endogenously from *Schizosaccharomyces pombe* (*S. pombe*) and human cells, together with structures of yeast pre-60S intermediates bound by the native complex. We compare the architectures of the yeast and human holoenzymes, define the multivalent interfaces that couple the scaffold to the catalytic core, show that these interfaces are required for both ITS2 processing and heterochromatin silencing, and demonstrate that assembly with the

scaffold enhances the activity of the nuclease–kinase module. We then describe how the scaffold anchors the complex on the pre-60S particle while the catalytic core remains flexible. Together, these data identify the scaffold as a functional organizer of the rixosome, coupling multivalent assembly to catalytic competence.

Results

Architecture of the intact *S. pombe* rixosome

To determine the near-physiological architecture of the rixosome, free of the confounding effects of recombinant overexpression or subcomplex dissociation, we purified the endogenous complex from *S. pombe* using an affinity tag-based strategy (Fig. 1A; fig. S1, D and E). All five expected core subunits (Las1, Grc3, Rix1, Ipi1, and Crb3) co-eluted in stoichiometric proportions, as confirmed by SDS-PAGE and mass spectrometry (Fig. 1A; fig. S1F).

Single-particle cryo-EM analysis revealed that the *S. pombe* rixosome (*Sp*Rixosome) is a ~1-MDa complex of 16 polypeptides with a Rix1:Crb3:Ipi1:Las1:Grc3 stoichiometry of 4:4:4:2:2. A twofold-symmetric $Las1_2$–$Grc3_2$ heterotetramer occupies the center of the assembly, flanked on opposite faces by two $Rix1_2$–$Crb3_2$–$Ipi1_2$ RIX scaffold modules (RIX^I and RIX^{II}). The two modules are not equivalent: RIX^I engages the core rigidly and was resolved at high resolution (2.68 Å; Fig. 1E; figs. S2 and S5, A and B), whereas RIX^{II} is flexibly tethered (Fig. S5C) and appears only as diffuse density. The intact complex is therefore compositionally symmetric but structurally only pseudo-twofold-symmetric (Fig. 1C).

Each RIX scaffold adopts a pronounced horseshoe architecture (Fig. 1D). A central Rix1 homodimer forms the structural core, with the two Crb3 β-propeller domains positioned at the dimer interface and Ipi1 at the periphery. The C-terminal regions of Crb3 extend toward the catalytic core through the central cavity of the Rix1 dimer, where they may contribute to scaffold–core association, whereas only the C-terminal region of Ipi1 could be modeled owing to limited local density. A similar horseshoe architecture has been observed in *Saccharomyces cerevisiae* (*S. cerevisiae*) and *Tetrahymena thermophila* (*T. thermophila*), suggesting that the overall scaffold organization is conserved across divergent eukaryotes (*10*, *29*).

A hierarchical refinement workflow combining focused optimization and mask-based classification yielded a reconstruction of the catalytic module at 3.01 Å resolution, with side-chain features clearly resolved throughout the Las1 HEPN domains and the Grc3 PNK active sites (Fig. S5A). The twofold symmetry of this module is geometrically matched to the two flanking RIX scaffolds, accounting for the overall organization of the holoenzyme.

A distinct conformational state of the RNase–PNK catalytic module in the intact *S. pombe* rixosome

Within the intact *S. pombe* rixosome, the two Las1 protomers of the catalytic heterotetramer meet through their HEPN domains to form the dimer interface. Density is best defined for these domains, and most of Grc3 is also resolved (Fig. 2A). The conserved catalytic

residues of the Las1 HEPN active site—R117, H118, and H122—are assigned unambiguously (Fig. 2A, inset). The Grc3 clasp motif lies adjacent to the Las1 active site, enabling efficient transfer of the substrate from Las1 to Grc3 for sequential processing.

To define the conformational state of the RNase–PNK core within the intact rixosome, we compared it with previously reported structures of the isolated *Chaetomium thermophilum (C. thermophilum)* RNase–PNK, which captured the catalytic core in two ATP-γS-bound states, nuclease-ready (state 1) and kinase-ready (state 2) (*25*). Superposition of our structure onto both states reveals a highly conserved catalytic core whose dimeric assembly is preserved within the intact complex (Fig. 2B), in agreement with previously determined RNase–PNK structures (*13*, *16*). Closer inspection, however, shows that key catalytic residues deviate from both reference states: relative to the nuclease-ready state (state 1), H118 of Las1 is markedly reoriented, whereas relative to the kinase-ready state (state 2), the W455 clasp of Grc3 swings away from the catalytic cleft (Fig. 2B). The RNase–PNK core in the intact *S. pombe* rixosome therefore does not simply resemble either previously defined state; instead, its HEPN active site and Grc3 clasp adopt a distinct conformational configuration. That both elements deviate from the previously reported nuclease- and kinase-ready states suggests that these conformational transitions are more varied than previously appreciated.

Architecture of the intact human rixosome

To extend this analysis to a multicellular eukaryote, we purified the intact endogenous human rixosome (*Hs*Rixosome) from HeLa cells carrying a Flag-GFP tag knocked into the

native NOL9 locus and determined its high-resolution cryo-EM structure (Fig. 3, A to D; figs. S1, A to C and S3A). Locally refined maps of the scaffold and catalytic modules reached 2.65 and 3.23 Å, respectively (Fig. S6B).

The human complex, spanning approximately 186 × 145 × 149 Å, comprises a single PELP1–TEX10–WDR18 scaffold module bound to one face of the LAS1L–NOL9 catalytic heterotetramer (Fig. 3, C and D). The opposite face of the catalytic core is not occupied by scaffold in our reconstruction, a point we return to in the Discussion.

In the human catalytic module, the LAS1L HEPN domains form a dimeric catalytic center, and the NOL9 kinase domains assemble complete nucleotide-binding pockets that define a 5′-end substrate entry channel. The NOL9 C-terminal domain (CTD) was too flexible to model de novo, but an AlphaFold-predicted model fits the weak density (Fig. S7, A and B).

The intact complex also differs from reconstituted subcomplexes. Its scaffold closely resembles the previously reported PELP1–WDR18 complex, consistent with a conserved scaffold organization, but the endogenous holoenzyme contains a single TEX10 molecule, in contrast to the predominantly 2:2:2 PELP1–WDR18–TEX10 organization observed upon in vitro reconstitution (*26*). Within the holoenzyme, this TEX10 contacts the scaffold and directly engages the catalytic module, placing it at the scaffold–core interface and supporting its role as an architectural bridge between the two modules.

The human structure also reveals a marked repositioning of TEX10 relative to its yeast homolog. TEX10 sits at the center of the scaffold–core interface, contacting NOL9, WDR18, and LAS1L simultaneously (Fig. 3D). This distinct positioning places TEX10 where it can integrate scaffold–core interactions with additional functions of the human rixosome.

Mass spectrometry of our preparations additionally identified SENP3 and MDN1, factors previously linked to the human complex, but no density corresponding to either appears in our maps, consistent with substoichiometric or highly flexible association (Fig. 3A).

Multivalent anchoring couples scaffold and catalytic modules in both species

Having established the overall architectures, we next defined the molecular basis of scaffold–core coupling. In the yeast complex, the high-resolution maps show that the RIX[1] scaffold engages the catalytic module not through a single dominant interface but through a distributed network of contact sites (Fig. 4A).

The first anchoring site is an extensive hydrophobic interface in which Crb3 engages a complementary patch on Grc3: Crb3 I74 packs against Grc3 F436 and I440, with a polar interaction between Crb3 R56 and Grc3 N437 providing secondary reinforcement (Fig. 4B). The second anchoring site is a potential salt bridge between Rix1 R140 and Las1 D31 in the HEPN catalytic domain (Fig. 4C). Sequence-conservation analysis combined with AlphaFold3 modeling identified a third, auxiliary contact, in which a coiled-coil

region of Las1 is predicted to engage a conserved helical bundle of Crb3—the coiled-coil-binding domain (CBD) whose WDR18 homolog forms the cognate contact with LAS1L in the human complex (Fig. S8, A and B). This region shows weak cryo-EM density, consistent with conformational flexibility, but the predicted model is compatible with the low-resolution features and supports its role as a dynamic connector between the modules.

To test whether either major interface is required for complex integrity, we introduced point mutations at the two anchoring sites (Rix1-R140F, Crb3-I74A/Q), individually and in combination. None of the mutants dissociated: all migrated as intact >1-MDa species indistinguishable from wild type on native PAGE (Fig. S8C). No single anchoring site is therefore required for rixosome integrity; instead, multiple scaffold–core contacts appear to stabilize the holoenzyme collectively.

The human complex reveals the same principle. Coupling between the scaffold and the LAS1L–NOL9 core is likewise distributed across multiple structurally distinct contacts (Fig. 4D). One major site is an electrostatic network between WDR18 and NOL9, centered on a potential salt bridge between WDR18 E347 and NOL9 K459 (Fig. 4E). A second engages a conserved PELP1 loop (residues 246–254) and the HEPN domain of LAS1L, with PELP1 F250 and L254 inserting into a hydrophobic groove centered on LAS1L V56 (Fig. 4F). A third, auxiliary contact is formed by the LAS1L coiled-coil, which is predicted to engage the CBD of WDR18. This interface is not resolved at high resolution; the AlphaFold3-predicted model, rigid-body docked into the low-pass-filtered map, is compatible with the weak density in this region (Fig. S7, A and B). Together with the two

major sites, this auxiliary contact shows that the coupling strategy is conserved at the level of molecular logic, even though the participating residues and secondary-structure elements differ substantially between species: multiple discrete contacts of mixed hydrophobic and electrostatic character collectively integrate the scaffold with the catalytic core.

Assembly with the scaffold enhances the catalytic activity of the nuclease–kinase module

We next asked whether assembly with the scaffold influences the intrinsic catalytic activity of the RNase–PNK module. In cleavage assays with a 5′-Cy5-labeled truncated *Sp*ITS2 substrate, the intact *Sp*Rixosome processed RNA robustly at low nanomolar concentrations (2.5–10 nM), generating two sequential cleavage products of defined length (Fig. 5A). By contrast, the isolated recombinant RNase–PNK heterotetramer was essentially inactive under identical conditions (10 nM). ATP-hydrolysis and kinase assays likewise showed markedly higher ATP-to-ADP conversion by the intact complex than by the isolated module across the concentration range tested (1 nM–1 μM) (Fig. 5B). Given the established nuclease–kinase mechanism, in which Grc3 programs Las1 for specific cleavage and the two HEPN active sites act in concert (*13*, *14*, *18*), these observations indicate that the scaffolded architecture is required for efficient coupled cleavage and phosphorylation in vitro.

To investigate how the scaffolded architecture might facilitate substrate engagement, we docked an ITS2 RNA fragment onto the RNase–PNK module using HDOCK (*30*). The resulting model places the RNA within the channel between the RIX

scaffold and the catalytic core, with its trajectory extending toward the Las1 HEPN active site (Fig. S9).

Scaffold–core interfaces are required for efficient ITS2 processing and chromatin silencing

We next tested whether the identified interfaces are functionally required for the two principal activities of the rixosome: ITS2 processing during ribosome biogenesis and heterochromatin-mediated transcriptional silencing. ITS2 processing depends on the sequential and tightly coupled activities of the Las1 endonuclease and the Grc3 kinase (Fig. S10, A and B): Las1 cleaves ITS2 to generate a 5′-OH terminus, which Grc3 subsequently phosphorylates to produce a 5′-phosphate, enabling exosome-mediated 3′→5′ trimming of the 7S pre-rRNA (*17*, *18*, *21–23*) . Northern blot analysis revealed that disruption of either the Rix1–Las1 interface (Rix1-R140F) or the Crb3–Grc3 interface (Crb3-I74A/Q) caused pronounced accumulation of the 7S pre-rRNA intermediate (Fig. 5C). These mutants also showed a modest increase in the 26S pre-rRNA, but the much stronger accumulation of 7S is consistent with reduced efficiency of the coupled cleavage–phosphorylation reaction rather than a complete block in downstream maturation. Because Crb3 I74 engages Grc3 F436 and I440 whereas Rix1 R140 contacts Las1 D31 (Fig. 4, B and C), disrupting either interface is expected to perturb the structural connection between the scaffold and the catalytic components, reducing the efficiency of their coupled activities. The scaffold therefore functions not as a passive assembly platform but as an active structural element that coordinates the relative positioning of the nuclease and kinase modules.

These interfaces also contribute to heterochromatin function. At the *S. pombe* mating-type (*mat*) locus, the rixosome is required to maintain transcriptional silencing of the *mat2P* and *mat3M* cassettes; loss of rixosome function leads to derepression, mating-type switching, and sporulation, which can be monitored by iodine staining (*6*, *24*, *31–34*) (Fig. 5D). Disruption of either interface individually produced only weak iodine staining, indicating that perturbing a single interface has a limited effect on silencing, whereas simultaneous disruption of both produced strong staining, revealing pronounced genetic synergy (Fig. 5D). The two interfaces therefore make overlapping contributions to rixosome-dependent silencing: individual contacts can partially compensate for one another, but their cumulative loss substantially compromises function. This redundancy-cum-synergy is the signature of multivalent anchoring and provides a robust structural basis for maintaining rixosome-dependent chromatin silencing.

The rixosome remains scaffold-anchored after ITS2 removal

To determine how the rixosome acts on ITS2 and when it is released, we reconstituted endogenous *Sp*Rixosome with native pre-60S particles purified by Rsa4-NTS affinity isolation. This captured several previously unobserved rixosome-bound intermediates, including two states that differ in whether the ITS2 foot is present (Fig. 6, A and B). In the foot-present state, the RIX scaffold is stably anchored on the pre-60S ribosome adjacent to the ITS2 foot, density for the ITS2 5′ region is visible, and Nop53—the adaptor that recruits the Mtr4–exosome for ITS2 degradation (*35*, *36*)—is bound at the base of the foot (Fig. 6A). In the foot-absent state, both the ITS2-foot density and Nop53 are no longer detectable, yet the RIX scaffold remains bound at the same site (Fig. 6B). The rixosome

297 therefore stays engaged with a pre-60S particle after its ITS2 substrate and the associated
298 processing factors have been cleared. This configuration, not previously visualized, places
299 rixosome release late in maturation.
300
301 Across all resolved states, the scaffold and catalytic modules behaved differently.
302 The RIX scaffold remained well resolved and consistently adjacent to the ITS2 foot,
303 providing a stable structural reference, whereas the RNase–PNK catalytic module and the
304 second RIX module (RIX^{II}) displayed variable orientations and reduced local resolution
305 that required recentering and local refinement for recovery. This asymmetry suggests a
306 division of labor: the scaffold establishes a geometrically defined docking platform on the
307 pre-60S surface, while the catalytic core retains the conformational flexibility needed to act
308 on a moving substrate. The rixosome engages the particle while retaining the twofold-
309 symmetric architecture of the free complex (Fig. 6A), indicating that the global architecture
310 is preserved upon binding.
311
312 **A unified model for rixosome action during ribosome biogenesis**
313 Our structural and functional data support a mechanistic model for rixosome-mediated
314 ITS2 processing (Fig. 6C). During 5S RNP rotation and pre-60S remodeling, the RIX
315 scaffold first docks the complex near the ITS2 foot, establishing a stable spatial reference
316 frame. Subsequent conformational maturation of the pre-60S particle then exposes ITS2 to
317 the RNase–PNK catalytic core, enabling stepwise endonucleolytic cleavage and
318 phosphorylation within the geometrically constrained channel formed at the scaffold–core
319 interface. Once the exosome completes ITS2 degradation and the ITS2 foot-associated

factors dissociate, the structural constraints that retained the rixosome are relaxed, permitting the complex to disengage. This coupling of stable scaffold anchoring with catalytic flexibility allows the rixosome to coordinate RNA processing with the structural maturation of the pre-60S particle in a spatially and temporally controlled manner. Collectively, this model integrates multivalent scaffold–core anchoring, scaffold-dependent enhancement of catalysis, and staged, scaffold-anchored engagement of the pre-60S particle into a single framework for rixosome action.

Discussion

Our structures establish a conserved architectural framework for the eukaryotic rixosome while revealing substantial plasticity in its peripheral scaffold. Across *S. pombe* and human, the Las1–Grc3 catalytic core is conserved, whereas the peripheral RIX scaffold differs. Previous work had defined isolated human subcomplexes—the PELP1–WDR18–TEX10 scaffold and the LAS1L–NOL9 catalytic module—and low-resolution views of rixosome-associated pre-60S particles (*26*, *27*, *37*). Here, structures of intact, endogenously purified holoenzymes from two divergent eukaryotes define the multivalent scaffold–core interfaces, show genetically that these interfaces are required for both ITS2 processing and heterochromatin silencing, demonstrate that assembly with the scaffold enhances the activity of the nuclease–kinase module, and capture the native complex bound to pre-60S intermediates. Together with the accompanying biochemical and genetic data, they provide the framework for interpreting how scaffold organization governs catalysis in intact rixosomes.

The RIX scaffold contributes directly to the functional organization of the RNase–PNK module rather than merely stabilizing it. Relative to the isolated module, RIX engagement is associated with distinct conformations of the Grc3 PNK domain around W455 and of the Las1 HEPN domain, and the intact complex is markedly more active than the isolated module in both cleavage and kinase assays. Two non-mutually exclusive models could account for this enhancement. In an allosteric model, scaffold binding alters the relative orientation of the Las1 HEPN domains and the Grc3 PNK active site, favoring a catalytically competent configuration. In a substrate-recruitment model, the scaffold increases the local concentration or residence time of the substrates near the catalytic core, potentially through the electropositive channel identified in our docking analysis. Our activity measurements establish that the scaffold is functionally required, but they do not distinguish between these possibilities; doing so will require RNA-binding measurements and structures of substrate-bound or reaction-trapped complexes to define how RNA is positioned during catalysis. Together with the requirement for scaffold–core contacts in ITS2 processing and silencing in vivo, these observations place the scaffold in a position to coordinate catalytic organization with substrate access.

In addition to these conserved features, the scaffold module is organized differently in the two species. In *S. pombe*, Ipi1 is predominantly associated with the pre-60S ribosome, with its C-terminal domain connecting it to the RIX scaffold, whereas human TEX10 sits directly at the scaffold–core junction, contacting NOL9, WDR18, and LAS1L simultaneously. The centralization of TEX10 at this junction, in place of the peripheral position of yeast Ipi1, may reflect the integration of scaffold–core assembly with functions

beyond ribosome biogenesis, such as recruitment of the human rixosome to Polycomb target genes through a TEX10–RING1B interaction (*7*).

The stoichiometry of the scaffold differs between the two reconstructions as well. The yeast holoenzyme consistently assembles with two RIX modules—one rigidly engaged and one flexibly tethered—both free and on the pre-60S ribosome, whereas our endogenous human reconstruction captures a single-scaffold state. The human rixosome is nevertheless likely to be bilateral as well: low-resolution in-cell cryo-ET has visualized the intact human rixosome bridging two pre-60S particles (*37*), and weak, ill-defined density on the face of the catalytic core opposite the modeled module in our 2D class averages is consistent with a second, flexibly associated scaffold module.

The two modules show a clear division of labor on the pre-60S ribosome: the scaffold forms a stable docking platform at the ITS2 foot, while the catalytic core retains the conformational plasticity needed to act on a moving substrate. Low-resolution in situ structures have visualized the intact human rixosome on pre-60S particles (*37*), indicating that scaffold-anchored engagement is not restricted to yeast; higher-resolution structures of the human rixosome–pre-60S complex will be needed to establish how closely its binding geometry matches that defined here for *S. pombe*. Our structures further indicate that rixosome release is temporally separable from remodeling of the ITS2-foot/Nop53-associated region: the scaffold persists through this remodeling, showing that rixosome engagement extends beyond the initial processing event and into the maturation of subsequent intermediates.

The interfaces defined here bear on how disease-associated LAS1L variants may act. Reported mutations are concentrated in the catalytic module and in the CC (coiled-coil) domain (Fig. S11), placing disease-associated variation in regions involved in catalysis and in scaffold–core organization. HEPN-domain mutations are expected to compromise endonucleolytic cleavage directly, whereas CC-domain mutations may weaken the auxiliary LAS1L–WDR18 contact and thereby reduce the efficiency of coordinated cleavage and phosphorylation. The phenotypic spectrum associated with LAS1L dysfunction may therefore reflect distinct effects on these catalytic and architectural functions.

Multivalent anchoring is not unique to the rixosome: the same strategy shapes other large RNP machines, including the spliceosome, the exosome, and the SAGA coactivator complex, in which stable assembly emerges from the cumulative effect of many weak-to-moderate-affinity interactions (*38–42*). For a dual-function complex such as the rixosome, this architecture is well matched to the variable mechanical and chemical environments of ribosome biogenesis and chromatin engagement, while the sensitivity of individual interfaces to perturbation offers potential regulatory entry points.

Several questions remain open. Our structures are static snapshots that do not capture RNA-engaged conformations, so structures with ITS2 substrates or trapped intermediates will be needed to define the complete catalytic cycle. The structural basis and stoichiometry of interactions with factors such as MDN1 and SENP3 likewise await direct visualization. Finally, because the functional perturbations in this study were performed in

S. pombe, testing the corresponding scaffold–core interfaces in human ribosome biogenesis and Polycomb-associated regulation will determine the extent to which these mechanisms are conserved.

Together, our structures define the rixosome as a conserved catalytic complex built on a structurally adaptable scaffold, in which a stably anchored module positions and activates a flexible catalytic core. This organization provides a foundation for understanding how mutations in human rixosome components, including LAS1L in Wilson–Turner syndrome, lead to tissue-specific pathology (*11*).

Methods

Flag-GFP-NOL9 cell line generation

To generate a HeLa Flag-GFP-NOL9 cell line, a DNA repair template was designed to introduce a tandem Flag-GFP tag at the N terminus of endogenous NOL9. The repair cassette contained a hygromycin-resistance selection marker and the Flag-GFP tag linked by a cleavable P2A sequence, and was flanked by two homology arms of approximately 800 bp on each side of the Cas9 cut site in the first exon of NOL9. The repair template was cloned into a pCAG plasmid backbone and verified by Sanger sequencing. The 20-bp sgRNA target sequence 5'-TCGGGACTGCTGCTAAAGCG-3' (PAM: GGG) was selected using the Benchling CRISPR design tool and inserted into a modified pX459 V2.0 plasmid (Addgene #62988) expressing 2×NLS-monomeric streptavidin (mSA)-tagged Cas9 and chimeric gRNA.

For transfection, 2.5 μg of total DNA, consisting of equimolar amounts of the in-house-prepared 3′-biotin-labeled single-stranded DNA repair template and the Cas9/gRNA plasmid, was transfected into 2×10^5 HeLa cells in a 6-well plate using Lipofectamine 2000 (Thermo Fisher Scientific) in 2.5 mL Opti-MEM medium. After 4 hours, the transfection medium was replaced with DMEM supplemented with 10% FBS.

Cells were allowed to recover for 24 hours and then expanded into four wells of a new 6-well plate for the first round of selection. Puromycin was applied for at least 5 days to enrich transfected cells. Once the surviving cells reached full confluence, they were expanded again for a second round of selection with hygromycin to enrich knock-in cells. GFP-positive cells

were isolated by fluorescence-activated cell sorting (FACS) after expansion to full confluence in 6-cm dishes. Single-cell clones were screened by PCR and Sanger sequencing to confirm precise integration of the Flag-GFP tag at the N terminus of NOL9. Expression of Flag-GFP-NOL9 was further validated by western blotting.

Yeast strains generation

To generate the Flag-Crb3 yeast strain, we designed the homologous DNA repair template, encoding the affinity tag (3C-cleavable Flag) carrying the ADH1 promoter downstream of the hphMX6 module. The insert was flanked by about 300 bp of homology on either side of the region immediately downstream of the Crb3 start codon. The cassette was cloned into a pCAG plasmid backbone for Sanger sequencing. The double-stranded DNA repair template was then amplified from the constructs, and transformed into the wild-type haploid strain (LD331), according to the manufacturer's instructions provided with the commercial kit (Coolaber). Finally, single positive clones were confirmed by PCR and western blot analysis.

The *S. pombe* strains used for functional studies, including both in vitro and in vivo assays, were derived from diploid strains (Genotype: h+/h- ade6-M210/ade6-M216 leu1-32/leu1-32 ura4-D18/ura4-D18). They were constructed using standard methods for transformation, mating, sporulation and tetrad dissection and are listed below. Chromosomally tagged strains were constructed using a PCR-based integration strategy(*43*, *44*). Standard cloning was used throughout. Yeast was grown in YES medium, unless otherwise indicated.

Genotypes of the *S. pombe* strains used in functional studies:

$Crb3^{WT}$: adh1p-Flag-crb3::bsdMX6

$Crb3^{I74A}$: adh1p-Flag-crb3-I74A::bsdMX6

$Crb3^{I74Q}$: adh1p-Flag-crb3-I74Q::bsdMX6

$Rix1^{WT}$: rix1-Twin-Strep::kanMX6

$Rix1^{R140F}$: rix1-R140F-Twin-Strep::kanMX6

$Crb3^{WT}$ $Rix1^{WT}$: adh1p-Flag-crb3::bsdMX6; rix1-Twin-Strep::kanMX6

$Crb3^{I74A}$ $Rix1^{R140F}$: adh1p-Flag-crb3-I74A::bsdMX6; rix1-R140F-Twin-Strep::kanMX6

$Crb3^{I74Q}$ $Rix1^{R140F}$: adh1p-Flag-crb3-I74Q::bsdMX6; rix1-R140F-Twin-Strep::kanMX6

The Flag-Crb3::Twin-Strep-Rsa4 strain (genotype: adh1p-Flag-crb3::bsdMX6; rsa4-Twin-Strep::hphMX6) was generated by PCR-based chromosomal integration. A DNA cassette encoding a N-terminal Twin-Strep tag and hphMX6 selection marker was amplified with homology arms targeting the endogenous rsa4 locus and transformed into the Flag-Crb3 strain (adh1p-Flag-crb3::bsdMX6) using the same transformation procedure described above. Correct integration was confirmed by PCR and western blot analysis.

Purification of *Hs*Rixosome

Purification of *Hs*Rixosome was carried out using a sequential fractionation approach adapted from a previous study (*7*), with slight modification. Flag-GFP-NOL9 HeLa cells were cultured in complete medium in 15-cm dishes, when reaching full confluency, cells from 30 dishes were harvested, washed with PBS and frozen into liquid nitrogen for storage at -80 °C until further use.

Frozen cell pellets were resuspended in hypotonic buffer ① (10 mM HEPES pH 7.9, 10 mM NaCl, 1.5 mM $MgCl_2$, 1 mM DTT, 1 mM PMSF) and dounced (Pestle B) 7 times on ice. The resulting lysate was centrifuged and the supernatant discarded. The nuclei were then resuspended in buffer ② (50 mM HEPES pH 7.4, 150 mM NaCl, 1.5 mM $MgCl_2$, 0.5 mM EGTA, 0.1 % Triton X-100, 1 mM DTT, 1 mM PMSF, 3.9 mg/mL aprotinin, 2.1 mg/mL pepstatin and 15 mg/mL leupeptin), and centrifuged at 2,000 × g for 10 min to obtain a chromatin-enriched fraction. The crude chromatin pellet was resuspended in buffer ③ (50 mM HEPES pH 7.4, 250 mM NaCl, 1.5 mM $MgCl_2$, 0.5 mM EGTA, 1 % Triton X-100, 1 mM DTT, 1 mM PMSF, 3.9 mg/mL aprotinin, 2.1 mg/mL pepstatin and 15 mg/mL leupeptin), To ensure complete solubilization of nuclear acid-associated proteins, the lysate was incubated for 1 hour on a rotator at 4 °C. The soluble fraction was collected by centrifugation (4 °C, 14,000 rpm for 1 hour). The supernatant was incubated with anti-Flag resin (DYKDDDDK (G1), Genscript) for 3 hours at 4 °C, followed by five washes with Buffer ④ (50 mM HEPES pH 7.4, 250 mM NaCl, 1.5 mM $MgCl_2$, 0.5 mM EGTA, 0.02% GDN, 1 mM PMSF, 3.9 mg/mL aprotinin, 2.1 mg/mL pepstatin and 15 mg/mL leupeptin). The complexes were eluted using Buffer ④ supplemented with 0.2 mg/mL Flag peptide. The eluate was concentrated using a 100-kDa cut-off Centricon (Millipore) and followed by crosslinking in the presence of 1 mM bis [sulfosuccinimidyl] suberate (BS3, Sigma) at 4 °C for 1 hour. The crosslinked protein was applied to size-exclusion chromatography (Superose 6 Increase, 10/300 GL, Cytiva) in Buffer ④. The peak fractions containing the rixosome complex were pooled and concentrated for further experiments.

Purification of *Sp*Rixosome

Yeast cultures were grown to stationary phase and 6 L cells were collected by centrifugation and resuspended in 1/5 volume pellet buffer ③ (same as the purification of the *Hs*Rixosome). The cell suspension was dropped into liquid nitrogen to form yeast beads with a diameter of 3–6 mm and pulverized to powder by Retsch zm200 Freezer Mill. The frozen cell powder (from 6 L of yeast culture) was thawed at 4 °C and resuspended in buffer ③. To ensure complete solubilization of nuclear acid-associated proteins, the lysate was incubated for 1 hour on a rotator at 4 °C. The cell lysate was first centrifuged at 14,000 rpm for 1 hour. The supernatant was incubated with anti-Flag resin followed by five washes with Buffer ④ (same as the purification of the *Hs*Rixosome). The complexes were eluted using Buffer ④ supplemented with 0.2 mg/mL Flag peptide. The eluate was concentrated using a 100-kDa cut-off Centricon (Millipore) and followed by crosslinking in the presence of 1 mM BS3 at 4 °C for 1 hour. The crosslinked protein was applied to size-exclusion chromatography (Superose 6 Increase, 10/300 GL, Cytiva) in Buffer ④. The peak fractions containing the rixosome complex were pooled and concentrated for further experiments.

Purification of rixosome-bound pre-60S particles

Yeast cultures expressing Flag-tagged Crb3 and Twin-Strep-tagged Rsa4 were harvested and disrupted by cryogenic grinding using Freezer Mill. The resulting cell powder was thawed, resuspended in buffer ③, and incubated at 4 °C for 1 hour in the presence or absence of AMP-PNP. After clarification by centrifugation, the lysate was subjected separately to anti-

Flag and anti-Strep affinity purification to isolate rixosome and pre-60S particles, respectively.

Following washing, rixosome-containing complexes were eluted with Flag peptide, whereas pre-60S particles were eluted with D-biotin. The two eluates were mixed and incubated at 4 °C for 1 hour to allow assembly of pre-60S–rixosome complexes. Reconstituted particles were concentrated using centrifugal concentrators and subsequently analyzed by negative-stain EM and cryo-EM. For nucleotide-stabilized samples, AMP-PNP was added prior to vitrification.

RNA extraction and Northern Blot analysis

Yeast cultures were grown to exponential phase (OD600 = 1.2), and 4 OD600 units of cells were collected and washed with DEPC-treated H_2O. RNA was extracted from intact yeast cells using TES buffer and acidic phenol-chloroform at 65 °C for 1 hour with intermittent vortexing. The RNA was further purified by an additional acidic phenol extraction using phase-lock gel tubes (TIANGEN), followed by isopropanol precipitation according to standard procedures.

RNA electrophoresis and Northern blotting were performed as previously described (*45*). Total RNA and rRNA co-purified with *Sp*Rixosome complexes were resolved on 1% denaturing agarose gels. For whole-cell RNA samples, 5 μg of total RNA was loaded; for rRNA purified from *Sp*Rixosome complexes, 500 ng of RNA was loaded.

The following 3'-biotin-labeled oligonucleotide probes were used for Northern blot analysis. Probes adapted from previous studies or designed by this study are indicated:

18S probe: 5'-GCTTATACTTAGACATGCATGGCTTAATC-3'

5.8S probe: 5'-GTATCGCATTTCGCTGCGTTCTTCA-3'

ITS2a probe: 5'-CAAATTTTCGTTCAACACCTCATCAA-3'

ITS2b probe (CS153)56: 5'-CGTTAAGGTTCAAATATAAAAGAG-3'

28S probe: 5'-CCTGCGCTTATTGATATGCTTAAGTTCAGCGCG-3'

Western blotting

centrifugation at 1,000 × g for 5 min. Cell pellets were lysed in RIPA buffer (Beyotime) supplemented with 1 mM PMSF and 1 mM DTT. Lysis was performed on ice for 30 min, and lysates were clarified by centrifugation at 14,000 rpm for 10 min at 4 °C. Protein concentrations were determined using a BCA assay (Beyotime). Approximately 5 μg of protein from each sample was resolved on a 4–20% Bis-Tris gel (GenScript).

Yeast protein extracts were prepared by alkaline treatment as previously described57, with minor modifications. Briefly, 5 OD units of yeast cells were collected, resuspended in 500 μL distilled water, and treated with 0.7 M NaOH on ice for 20 min. Cells were pelleted by centrifugation at 13,000 rpm for 10 min at 4 °C, and the supernatant was carefully removed. Proteins were extracted from the pellet by adding 2–3 pellet volumes of 1× SDS sample buffer, followed by boiling at 99 °C for 10 min. Lysates were clarified by centrifugation at 14,000 rpm for 10 min at 4 °C before SDS-PAGE analysis. Proteins were transferred to a

PVDF membrane. The membrane was blocked in TBST containing 5% milk for 1 hour at room temperature and then incubated with anti-Flag antibody (Proteintech, 1:4,000).

For BN-PAGE analysis, the protocol was adapted from a previously described method with minor modifications (*46*). Briefly, 10–30 μg of Flag-affinity-purified *Sp*Rixosome or *Sp*Rixosome mutant complex was loaded onto a homemade 6–15% BN-PAGE gel. Electrophoresis was first performed at a constant voltage of 100 V until the samples entered the gel, followed by electrophoresis at a constant current of 15 mA for 2 hours. Proteins were transferred to a PVDF membrane in a cold room at 364 mA for 2.5 hours. The membrane was incubated with anti-Strep antibody (Abclonal, 1:2,000) to detect rixosome variants.

Cryo-EM grid preparation and data collection

For cryo-EM sample preparation, 3.5 μL of the purified protein sample (0.1-0.5 mg/mL) was loaded onto glow-discharged Cu grids coated with 2 nm carbon film (Quantifoil R1.2/1.3, 300 mesh). Grids were blotted for 3 s and plunge-frozen in liquid ethane using a Vitrobot Mark IV (Thermo Fisher Scientific) operated at 8 °C and 95% humidity.

Cryo-EM data were collected on a Titan Krios transmission electron microscope (Thermo Fisher Scientific) operated at 300 kV and equipped with a 20-eV energy filter and a Gatan K3 direct electron detector. Micrographs were recorded using AutoEMation at a nominal magnification of 81,000×, corresponding to a calibrated pixel size of 1.087 Å per pixel. Data were collected with a defocus range of −1.4 to −2.0 μm, a total electron dose of 50 e/Å^2.

Cryo-EM data processing

The data processing workflow for the rixosome and pre-60S particles is illustrated in fig. S2–S4. All steps were conducted in CryoSPARC v4 and RELION (*47–50*). For *Sp*Rixosome, a total of 11,591 micrographs were collected. Using the template picker, 3,096,991 particles were automatically selected. After particle extraction, multiple rounds of 2D classification, ab initio reconstruction, and heterogeneous refinement were performed, resulting in a dataset of 753,165 particles (consensus reconstruction, 2.97 Å). These particles were subjected to non-uniform refinement with C1 symmetry. To improve the reconstruction, additional rounds of 3D classification and heterogeneous refinement were performed on the initial particle stack, yielding 2,226,259 particles corresponding to the two-module assembly; non-uniform refinement with relaxed C2 symmetry gave a reconstruction of this assembly at 3.12 Å. In parallel, the predominant particle class (305,039 particles) containing a single RIX module and the catalytic heterotetramer—hereafter *Sp*Rixosome-RIX^{I}-only, the form used for high-resolution model building—was refined in C1 to 2.85 Å. To further improve local map quality, a hierarchical focused-refinement strategy was employed. First, a mask encompassing the RIX^{I} scaffold module and the RNase–PNK catalytic core was applied for local refinement. Subsequently, independent masks were generated for the RIX^{I} module and the RNase–PNK core, followed by additional rounds of focused refinement. The resulting locally refined maps were combined to generate a high-resolution composite map, with local resolutions reaching 2.68 Å for the RIX module and 3.01 Å for the RNase–PNK catalytic core.

For *Hs*Rixosome, a total of 24,927 micrographs were collected. After particle picking and extraction, multiple rounds of 2D classification, ab initio reconstruction, and heterogeneous refinement were performed, resulting in a final dataset of 139,083 particles. Non-uniform refinement of this particle stack yielded an initial high-resolution reconstruction. The particles were subsequently exported to RELION v3 (*50*) for polishing and further refinement, producing an overall map at 2.69 Å resolution. To enhance the quality of individual regions, focused refinements were carried out using masks corresponding to the RIX scaffold module and the RNase–PNK catalytic core. These locally refined maps were then combined into a composite reconstruction with resolutions of 2.65 Å and 3.23 Å, respectively.

For the *S. pombe* pre-60S dataset, a total of 40,436 micrographs were collected. Automated particle picking followed by reference-free 2D classification yielded 3,296,671 particles, and non-uniform refinement produced an initial consensus reconstruction at 2.30 Å. Further 3D classification resolved two major classes corresponding to the pre-5S rotation pre-60S ribosome with (1,411,416 particles, 2.20 Å) and without (382,184 particles, 2.33 Å) the ITS2 foot, together with a minor particle subset (~6%) carrying rixosome density. Within this subset, 3D classification separated two rixosome-containing states that, after non-uniform refinement and global and local CTF refinement, yielded reconstructions with (2.70 Å) and without (2.83 Å) the ITS2 foot; focused local refinement of the Rix1 region gave maps at 3.19 Å and 3.59 Å, respectively. The minor subset was additionally re-centered and re-extracted, and further 3D classification yielded a class containing a relatively stable rixosome (26,165 particles, 3.14 Å). All resolutions were estimated using the gold-standard Fourier shell correlation 0.143 criterion with high-resolution noise substitution.

646

647 **Model building and structure refinement**

648 AlphaFold-predicted models of individual subunits were initially fitted into the cryo-EM
649 maps using UCSF ChimeraX (*51*) and subsequently adjusted manually in Coot v0.9.8.1 (*52*).
650 Regions lacking interpretable density were omitted from the final models (Fig. 1B and Fig.
651 2B). For regions exhibiting weak or low-resolution density that was insufficient for reliable
652 atomic model building, AlphaFold-predicted structures were docked into the maps in UCSF
653 ChimeraX to illustrate their approximate positions but were not included in subsequent model
654 refinement (Fig. S7).

655

656 Real-space refinement was performed in PHENIX (*53*) using phenix.real_space_refine with
657 secondary-structure and stereochemical restraints. To assess overfitting, refined models were
658 validated against independent half-maps following the gold-standard refinement procedure.
659 Statistics for model refinement and validation are provided in tables S1 to S4.

660

661 ***S. pombe* RNase-PNK expression and purification**

662 The coding sequence of *S. pombe* Las1 (*Sp*Las1) was cloned into a modified pET21b vector
663 containing an N-terminal Flag tag, whereas the coding sequence of *S. pombe* Grc3 (SpGrc3)
664 was cloned into a modified pET28a vector containing an N-terminal SUMO tag and a C-
665 terminal His_{10} tag. Recombinant plasmids were transformed into Escherichia coli Rosetta
666 (DE3) cells and cultured in LB medium at 37 °C until reaching an OD600 of 0.8–1.0. Protein
667 expression was induced with 0.2 mM IPTG, and cells were further grown at 16 °C overnight.

668

669 Cells expressing Flag-tagged SpLas1 and SUMO-tagged, His_{10}-tagged SpGrc3 were
670 harvested, washed with PBS, and resuspended in Buffer ① supplemented with 500 mM
671 NaCl and protease inhibitors. The cells were lysed by sonication and the lysate was clarified
672 by centrifugation at 14,000 rpm for 1 hour. The supernatant was incubated with anti-Flag
673 resin for 3 hours at 4 °C. Following extensive washing, the *Sp*RNase-PNK complex was
674 eluted with Flag peptide-containing buffer.
675
676 The eluate was concentrated and digested with 3C protease overnight at 4 °C. After removal
677 of precipitated material by centrifugation, the sample was applied to a Heparin column
678 (HiTrap^{TM} Heparin HP affinity 5 mL, Cytiva) and further purified by size-exclusion
679 chromatography (Superdex 200 Increase 10/300, Cytiva). Peak fractions containing the
680 *Sp*RNase-PNK complex were pooled and concentrated for subsequent biochemical studies.
681
682 **In vitro ADP-Glo assay**
683 In vitro kinase activity was measured using the ADP-Glo Kinase Assay kit (Promega)
684 according to the manufacturer's protocol, with minor modifications. Purified *Sp*Rixosome or
685 mutant complexes were diluted in reaction buffer containing 20 mM Tris-HCl pH 8.0, 150
686 mM NaCl, 2 mM β-mercaptoethanol, 20 mM $MgCl_2$, 0.1 mg/mL BSA, and 5% glycerol.
687 Protein samples were serially diluted twofold, typically from 0.5 μM to 0.24 nM.
688
689 Reactions were assembled in 384-well plates in a final volume of 5 μL and contained the
690 indicated concentration of protein, 0.4 μM RNA substrate, and 100 μM ultra-pure ATP.
691 Reactions were incubated at 37 °C for 1 hour. ATP hydrolysis was then stopped by adding 5

μL ADP-Glo reagent, and plates were incubated at room temperature for 40 min to deplete remaining ATP. Next, 10 μL Kinase Detection Reagent was added to each well, and plates were incubated at room temperature for 40 min to convert ADP to ATP and generate luminescence. Luminescence was recorded with an integration time of 0.25 s per well.

For each replicate, an ATP-to-ADP conversion standard curve was prepared in the same reaction buffer by mixing ATP and ADP while maintaining a total nucleotide concentration of 100 μM. ATPase activity was calculated from this standard curve and reported as ATP-to-ADP conversion.

Iodine staining

Wild-type and mutant strains, including Crb3I74A/Q, Rix1R140F, and the corresponding double mutants, were grown in YES medium until the OD600 reached approximately 5. Cells were collected, resuspended, and adjusted to OD600 values of 10. Aliquots of 1, 2, and 5 μL of each suspension were spotted onto EMM-N (Edinburgh Minimal Medium without Nitrogen) plates. Plates were incubated at 32 °C for 1 day to allow mating and sporulation, then exposed to iodine vapor for 5–10 min at room temperature and photographed immediately. Three independent colonies were examined for each genotype.

In vitro ITS2 RNA cleavage assays

For fluorescence-based cleavage assays, 1 μM 5′-Cy5-labeled ITS2 RNA (GENCEFE Biotech) was incubated with increasing concentrations of *Sp*RNase–PNK complex (10–500 nM) and *Sp*Rixosome (2.5–10 nM) in cleavage buffer containing 20 mM Tris–HCl (pH

7.5), 300 mM NaCl, and 1 mM TCEP at 37 °C for 1 h. Reactions were terminated by the addition of 2× RNA loading buffer, followed by heating at 75 °C for 5 min and immediate cooling on ice. Samples were then resolved on 20% urea-denaturing polyacrylamide gels in 1× TBE buffer at room temperature. Cleavage products were detected by fluorescence imaging (TANON).

Data availability

Atomic coordinates and EM maps of rixosome reported in this study (*Sp*Rixosome-RIX^{I}-only: 27WP and EMD-81516; *Hs*Rixosome: 27WQ and EMD-81517; *Sp*RIX^{I}: EMD-81500; *Sp*RNase-PNK: EMD-81503; *Sp*Rixosome (containing two RIX modules): EMD-81505; *Hs*RIX: EMD-81506; *Hs*RNase-PNK: EMD-81507; Pre-5S rotation Pre-60S (with ITS2 Foot): 28EB and EMD-81677; Pre-5S rotation Pre-60S (no ITS2 Foot): 28EC and EMD-81678; *Sp*Rixosome-bound Pre-60S (with ITS2 Foot): 28EA and EMD-81676; *Sp*Rixosome-bound Pre-60S (no ITS2 Foot): 28DZ and EMD-81675; *Sp*Rixosome-bound Pre-60S (recentered): EMD-81679, EMD-81681 have been deposited in the Protein Data Bank (http://www.rcsb.org) and the Electron Microscopy Data Bank (https://www.ebi.ac.uk/pdbe/emdb/).

References:

1. A. Vanden Broeck, S. Klinge, Eukaryotic Ribosome Assembly. *Annu Rev Biochem* **93**, 189–210 (2024).
2. S. Konikkat, J. L. Woolford, Principles of 60S ribosomal subunit assembly emerging from recent studies in yeast. *Biochem J* **474**, 195–214 (2017).
3. J. L. Woolford, S. J. Baserga, Ribosome biogenesis in the yeast Saccharomyces cerevisiae. *Genetics* **195**, 643–681 (2013).
4. E. Hurt, J. Cheng, J. Baβler, J. Iwasa, R. Beckmann, SnapShot: Eukaryotic ribosome biogenesis I. *Cell* **186**, 2282-2282.e1 (2023).
5. E. Hurt, J. Iwasa, R. Beckmann, SnapShot: Eukaryotic ribosome biogenesis II. *Cell* **187**, 1314-1314.e1 (2024).
6. G. Shipkovenska, A. Durango, M. Kalocsay, S. P. Gygi, D. Moazed, A conserved RNA degradation complex required for spreading and epigenetic inheritance of heterochromatin. *Elife* **9**, e54341 (2020).
7. H. Zhou, C. B. Stein, T. A. Shafiq, G. Shipkovenska, M. Kalocsay, J. A. Paulo, J. Zhang, Z. Luo, S. P. Gygi, K. Adelman, D. Moazed, Rixosomal RNA degradation contributes to silencing of Polycomb target genes. *Nature* **604**, 167–174 (2022).
8. H. Zhou, W. Feng, J. Yu, T. A. Shafiq, J. A. Paulo, J. Zhang, Z. Luo, S. P. Gygi, D. Moazed, SENP3 and USP7 regulate Polycomb-rixosome interactions and silencing functions. *Cell Rep* **42**, 112339 (2023).
9. A. Vanden Broeck, S. Klinge, Principles of human pre-60S biogenesis. *Science* **381**, eadh3892 (2023).
10. M. Thoms, B. Lau, J. Cheng, L. Fromm, T. Denk, N. Kellner, D. Flemming, P. Fischer, L. Falquet, O. Berninghausen, R. Beckmann, E. Hurt, Structural insights into coordinating 5S RNP rotation with ITS2 pre-RNA processing during ribosome formation. *EMBO Rep* **24**, e57984 (2023).
11. H. Hu, S. A. Haas, J. Chelly, H. Van Esch, M. Raynaud, A. P. M. de Brouwer, S. Weinert, G. Froyen, S. G. M. Frints, F. Laumonnier, T. Zemojtel, M. I. Love, H. Richard, A.-K. Emde, M. Bienek, C. Jensen, M. Hambrock, U. Fischer, C. Langnick, M. Feldkamp, W. Wissink-Lindhout, N. Lebrun, L. Castelnau, J. Rucci, R. Montjean, O. Dorseuil, P. Billuart, T. Stuhlmann, M. Shaw, M. A. Corbett, A. Gardner, S. Willis-Owen, C. Tan, K. L. Friend, S. Belet, K. E. P. van Roozendaal, M. Jimenez-Pocquet, M.-P. Moizard, N. Ronce, R. Sun, S. O'Keeffe, R. Chenna, A. van Bömmel, J. Göke, A. Hackett, M. Field, L. Christie, J. Boyle, E. Haan, J. Nelson, G. Turner, G. Baynam, G. Gillessen-Kaesbach, U. Müller, D. Steinberger, B. Budny, M. Badura-Stronka, A. Latos-Bieleńska, L. B. Ousager, P. Wieacker, G. Rodríguez Criado, M.-L. Bondeson, G. Annerén, A. Dufke, M. Cohen, L. Van Maldergem, C. Vincent-Delorme, B. Echenne, B. Simon-Bouy, T. Kleefstra, M. Willemsen, J.-P. Fryns, K. Devriendt, R. Ullmann, M. Vingron, K. Wrogemann, T. F. Wienker, A. Tzschach, H. van Bokhoven, J. Gecz, T. J. Jentsch, W. Chen, H.-H. Ropers, V. M. Kalscheuer, X-exome sequencing of 405 unresolved families identifies seven novel intellectual disability genes. *Mol Psychiatry* **21**, 133–148 (2016).
12. J. Gordon, M. C. Pillon, R. E. Stanley, Nol9 Is a Spatial Regulator for the Human ITS2 Pre-rRNA Endonuclease-Kinase Complex. *J Mol Biol* **431**, 3771–3786 (2019).

13. M. C. Pillon, M. Sobhany, M. J. Borgnia, J. G. Williams, R. E. Stanley, Grc3 programs the essential endoribonuclease Las1 for specific RNA cleavage. *Proc Natl Acad Sci U S A* **114**, E5530–E5538 (2017).
14. M. C. Pillon, K. H. Goslen, J. Gordon, M. L. Wells, J. G. Williams, R. E. Stanley, It takes two (Las1 HEPN endoribonuclease domains) to cut RNA correctly. *J Biol Chem* **295**, 5857–5870 (2020).
15. V. Anantharaman, K. S. Makarova, A. M. Burroughs, E. V. Koonin, L. Aravind, Comprehensive analysis of the HEPN superfamily: identification of novel roles in intra-genomic conflicts, defense, pathogenesis and RNA processing. *Biol Direct* **8**, 15 (2013).
16. J. Chen, H. Chen, S. Li, X. Lin, R. Hu, K. Zhang, L. Liu, Structural and mechanistic insights into ribosomal ITS2 RNA processing by nuclease-kinase machinery. *Elife* **12**, RP86847 (2024).
17. L. Gasse, D. Flemming, E. Hurt, Coordinated Ribosomal ITS2 RNA Processing by the Las1 Complex Integrating Endonuclease, Polynucleotide Kinase, and Exonuclease Activities. *Mol Cell* **60**, 808–815 (2015).
18. C. D. Castle, R. Sardana, V. Dandekar, V. Borgianini, A. W. Johnson, C. Denicourt, Las1 interacts with Grc3 polynucleotide kinase and is required for ribosome synthesis in Saccharomyces cerevisiae. *Nucleic Acids Res* **41**, 1135–1150 (2013).
19. C. D. Castle, E. K. Cassimere, C. Denicourt, LAS1L interacts with the mammalian Rix1 complex to regulate ribosome biogenesis. *Mol Biol Cell* **23**, 716–728 (2012).
20. E. Kitano, A. Hayashi, D. Kanai, K. Shinmyozu, J. Nakayama, Roles of fission yeast Grc3 protein in ribosomal RNA processing and heterochromatic gene silencing. *J Biol Chem* **286**, 15391–15402 (2011).
21. S. Schillewaert, L. Wacheul, F. Lhomme, D. L. J. Lafontaine, The evolutionarily conserved protein Las1 is required for pre-rRNA processing at both ends of ITS2. *Mol Cell Biol* **32**, 430–444 (2012).
22. L. Fromm, S. Falk, D. Flemming, J. M. Schuller, M. Thoms, E. Conti, E. Hurt, Reconstitution of the complete pathway of ITS2 processing at the pre-ribosome. *Nat Commun* **8**, 1787 (2017).
23. L. Tafforeau, C. Zorbas, J.-L. Langhendries, S.-T. Mullineux, V. Stamatopoulou, R. Mullier, L. Wacheul, D. L. J. Lafontaine, The complexity of human ribosome biogenesis revealed by systematic nucleolar screening of Pre-rRNA processing factors. *Mol Cell* **51**, 539–551 (2013).
24. S. Holla, J. Dhakshnamoorthy, H. D. Folco, V. Balachandran, H. Xiao, L.-L. Sun, D. Wheeler, M. Zofall, S. I. S. Grewal, Positioning Heterochromatin at the Nuclear Periphery Suppresses Histone Turnover to Promote Epigenetic Inheritance. *Cell* **180**, 150-164.e15 (2020).
25. M. C. Pillon, A. L. Hsu, J. M. Krahn, J. G. Williams, K. H. Goslen, M. Sobhany, M. J. Borgnia, R. E. Stanley, Cryo-EM reveals active site coordination within a multienzyme pre-rRNA processing complex. *Nat Struct Mol Biol* **26**, 830–839 (2019).
26. J. Huang, L. Tong, Molecular insights into the overall architecture of human rixosome. *Nat Commun* **16**, 3288 (2025).

27. J. Gordon, F. L. Chapus, E. G. Viverette, J. G. Williams, L. J. Deterding, J. M. Krahn, M. J. Borgnia, J. Rodriguez, A. J. Warren, R. E. Stanley, Cryo-EM reveals the architecture of the PELP1-WDR18 molecular scaffold. *Nat Commun* **13**, 6783 (2022).
28. C. Barrio-Garcia, M. Thoms, D. Flemming, L. Kater, O. Berninghausen, J. Baßler, R. Beckmann, E. Hurt, Architecture of the Rix1-Rea1 checkpoint machinery during pre-60S-ribosome remodeling. *Nat Struct Mol Biol* **23**, 37–44 (2016).
29. L. Kater, V. Mitterer, M. Thoms, J. Cheng, O. Berninghausen, R. Beckmann, E. Hurt, Construction of the Central Protuberance and L1 Stalk during 60S Subunit Biogenesis. *Mol Cell* **79**, 615-628.e5 (2020).
30. Y. Yan, H. Tao, J. He, S.-Y. Huang, The HDOCK server for integrated protein–protein docking. *Nat Protoc* **15**, 1829–1852 (2020).
31. S. L. Forsburg, N. Rhind, Basic methods for fission yeast. *Yeast* **23**, 173–183 (2006).
32. G. Thon, A. Cohen, A. J. Klar, Three additional linkage groups that repress transcription and meiotic recombination in the mating-type region of Schizosaccharomyces pombe. *Genetics* **138**, 29–38 (1994).
33. H. Ohtsuka, K. Imada, T. Shimasaki, H. Aiba, Sporulation: A response to starvation in the fission yeast Schizosaccharomyces pombe. *Microbiologyopen* **11**, e1303 (2022).
34. A. Vyas, A. V. Freitas, Z. A. Ralston, Z. Tang, Fission Yeast Schizosaccharomyces pombe: A Unicellular "Micromammal" Model Organism. *Curr Protoc* **1**, e151 (2021).
35. L. P. P. Cepeda, F. F. M. Bagatelli, R. M. Santos, M. D. M. Santos, F. C. S. Nogueira, C. C. Oliveira, The ribosome assembly factor Nop53 controls association of the RNA exosome with pre-60S particles in yeast. *J Biol Chem* **294**, 19365–19380 (2019).
36. F. F. M. Bagatelli, F. N. de Luna Vitorino, J. P. C. da Cunha, C. C. Oliveira, The ribosome assembly factor Nop53 has a structural role in the formation of nuclear pre-60S intermediates, affecting late maturation events. *Nucleic Acids Res* **49**, 7053–7074 (2021).
37. X. Zhao, Y. Hayashi, H. K. H. Fung, S. Cuylen-Häring, J. Mahamid, C. W. Müller, In-cell structures visualize human pre-ribosome assembly in the nucleolus. bioRxiv [Preprint] (2026). https://doi.org/10.64898/2026.06.01.729245.
38. M. C. Wahl, C. L. Will, R. Lührmann, The spliceosome: design principles of a dynamic RNP machine. *Cell* **136**, 701–718 (2009).
39. C. L. Will, R. Lührmann, Spliceosome structure and function. *Cold Spring Harb Perspect Biol* **3**, a003707 (2011).
40. M. A. Cvetkovic, J. P. Wurm, M. J. Audin, S. Schütz, R. Sprangers, The Rrp4-exosome complex recruits and channels substrate RNA by a unique mechanism. *Nat Chem Biol* **13**, 522–528 (2017).
41. Y. Han, J. Luo, J. Ranish, S. Hahn, Architecture of the Saccharomyces cerevisiae SAGA transcription coactivator complex. *EMBO J* **33**, 2534–2546 (2014).
42. V. M. Weake, J. L. Workman, SAGA function in tissue-specific gene expression. *Trends Cell Biol* **22**, 177–184 (2012).
43. C. Janke, M. M. Magiera, N. Rathfelder, C. Taxis, S. Reber, H. Maekawa, A. Moreno-Borchart, G. Doenges, E. Schwob, E. Schiebel, M. Knop, A versatile toolbox for PCR-based tagging of yeast genes: new fluorescent proteins, more markers and promoter substitution cassettes. *Yeast* **21**, 947–962 (2004).

44. M. Knop, K. Siegers, G. Pereira, W. Zachariae, B. Winsor, K. Nasmyth, E. Schiebel, Epitope tagging of yeast genes using a PCR-based strategy: more tags and improved practical routines. *Yeast* **15**, 963–972 (1999).
45. P. Leeds, S. W. Peltz, A. Jacobson, M. R. Culbertson, The product of the yeast UPF1 gene is required for rapid turnover of mRNAs containing a premature translational termination codon. *Genes Dev* **5**, 2303–2314 (1991).
46. I. Wittig, H.-P. Braun, H. Schägger, Blue native PAGE. *Nat Protoc* **1**, 418–428 (2006).
47. A. Punjani, J. L. Rubinstein, D. J. Fleet, M. A. Brubaker, cryoSPARC: algorithms for rapid unsupervised cryo-EM structure determination. *Nat Methods* **14**, 290–296 (2017).
48. P. B. Rosenthal, R. Henderson, Optimal determination of particle orientation, absolute hand, and contrast loss in single-particle electron cryomicroscopy. *J Mol Biol* **333**, 721–745 (2003).
49. S. Chen, G. McMullan, A. R. Faruqi, G. N. Murshudov, J. M. Short, S. H. W. Scheres, R. Henderson, High-resolution noise substitution to measure overfitting and validate resolution in 3D structure determination by single particle electron cryomicroscopy. *Ultramicroscopy* **135**, 24–35 (2013).
50. S. H. W. Scheres, RELION: implementation of a Bayesian approach to cryo-EM structure determination. *J Struct Biol* **180**, 519–530 (2012).
51. E. F. Pettersen, T. D. Goddard, C. C. Huang, E. C. Meng, G. S. Couch, T. I. Croll, J. H. Morris, T. E. Ferrin, UCSF ChimeraX: Structure visualization for researchers, educators, and developers. *Protein Sci* **30**, 70–82 (2021).
52. P. Emsley, K. Cowtan, Coot: model-building tools for molecular graphics. *Acta Crystallogr D Biol Crystallogr* **60**, 2126–2132 (2004).
53. P. D. Adams, P. V. Afonine, G. Bunkóczi, V. B. Chen, I. W. Davis, N. Echols, J. J. Headd, L.-W. Hung, G. J. Kapral, R. W. Grosse-Kunstleve, A. J. McCoy, N. W. Moriarty, R. Oeffner, R. J. Read, D. C. Richardson, J. S. Richardson, T. C. Terwilliger, P. H. Zwart, PHENIX: a comprehensive Python-based system for macromolecular structure solution. *Acta Crystallogr D Biol Crystallogr* **66**, 213–221 (2010).

Acknowledgements

This work was supported by grants from the National Key Research and Development Program of China (2024YFA0916903 to H.S.), the Zhejiang Provincial Natural Science Foundation (DQ24C050001 to H.S.), the Research Center for Industries of the Future (RCIF), Westlake University, and the Westlake Education Foundation (to H.S.). We thank the Cryo-EM Facility and the HPC Center of Westlake University for providing data collection and computation support, respectively. We thank Prof. Xiangwei He (Zhejiang University) for advice and technical support on fission yeast culture and hybridization, and Prof. Xiaochun Yu and Dr. Man Luo (Westlake University) for technical support on Northern blotting.

Author information

These authors contributed equally: Zijie Zheng & Shu Shu.

Authors and affiliations

Zhejiang Key Laboratory of Structural Biology, School of Life Sciences, Westlake University, Hangzhou, Zhejiang, China

Zijie Zheng, Shu Shu, Xiao Li, Yuechan Wang & Huaizong Shen

Westlake Laboratory of Life Sciences and Biomedicine, Hangzhou, Zhejiang, China

Zijie Zheng, Shu Shu, Xiao Li, Yuechan Wang & Huaizong Shen

Institute of Biology, Westlake Institute for Advanced Study, Hangzhou, Zhejiang, China

Zijie Zheng, Shu Shu, Xiao Li, Yuechan Wang & Huaizong Shen

School of Engineering, Westlake University, Hangzhou, Zhejiang, China

Shiqi Fan

Contributions

The project was conceived by H.S. Z.Z., S.S. and X.L. performed molecular cloning, protein purification, sample preparation, cryo-EM micrograph collection, and biochemical characterization. Z.Z., S.S., S.F., and Y.W. carried out cryo-EM data processing, structure determination, and model building. All authors contributed to data analysis. Z.Z., S.S., and H.S. wrote the manuscript with intellectual input from all authors.

Corresponding authors

Correspondence to Huaizong Shen.

Ethics declarations

Competing interests

The other authors declare no competing interests.

Figures

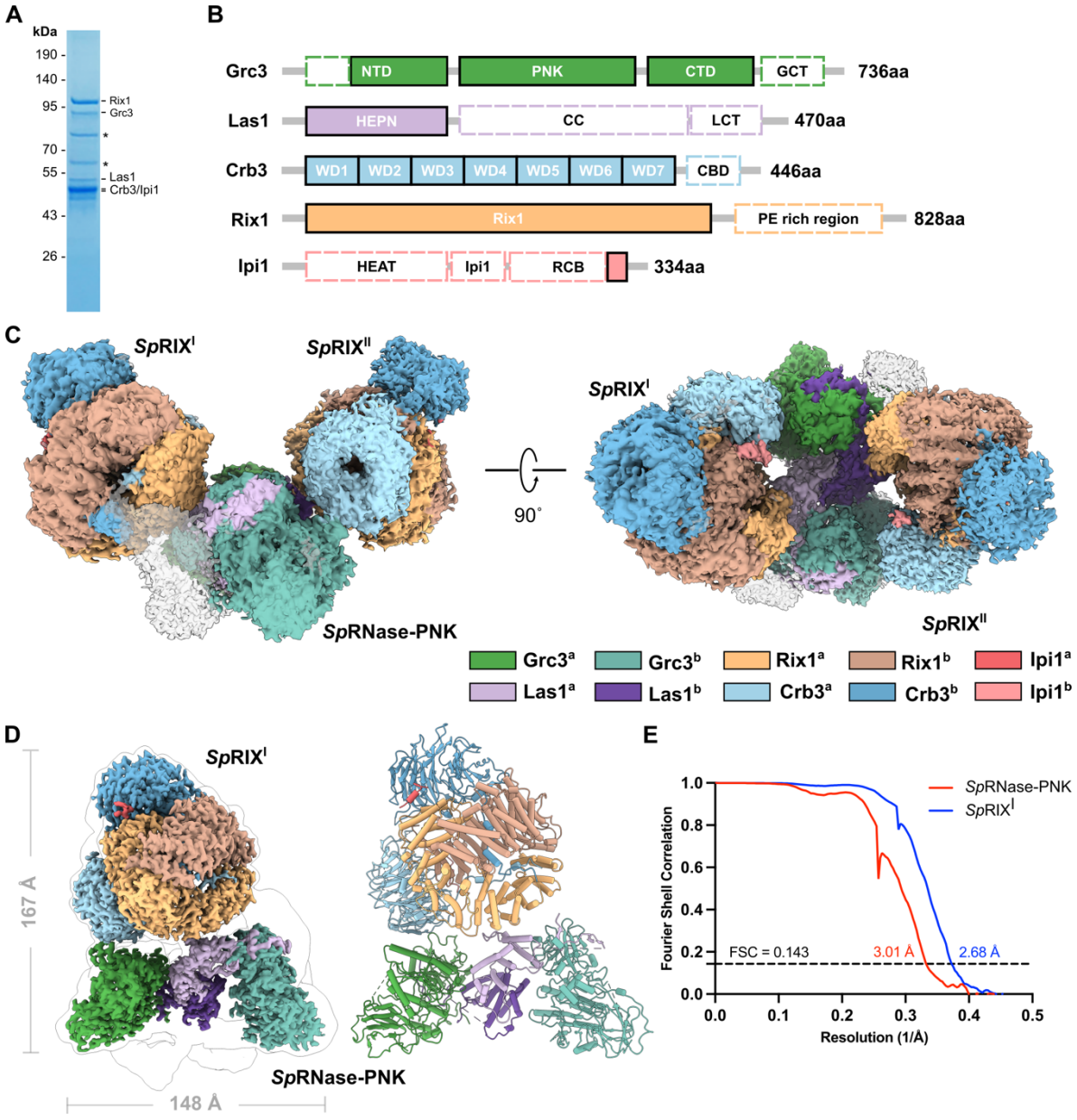

Fig. 1. Cryo-EM structure of the endogenous *S. pombe* rixosome. (**A**) SDS-PAGE analysis of the endogenously purified *S. pombe* rixosome (*Sp*Rixosome), with subunits labeled and identities confirmed by mass spectrometry. Asterisks mark unidentified minor bands. (**B**) Domain organization of the *Sp*Rixosome subunits. Dashed outlines indicate

regions not resolved in the reconstruction. GCT, Grc3 C-terminal tail; CC, coiled-coil; LCT, Las1 C-terminal tail; CBD, coiled-coil binding domain; RCB, Rix1–Crb3 binding domain. (**C**) Cryo-EM reconstruction of the *Sp*Rixosome in two orthogonal views related by a 90° rotation, showing the twofold-symmetric catalytic heterotetramer (RNase–PNK) flanked by one RIX scaffold module on each side; RIX^{I} is rigidly engaged whereas RIX^{II} is flexibly tethered. Subunits are color-coded. (**D**) Composite cryo-EM map (left) and corresponding atomic model (right) of the twofold-symmetric RNase–PNK catalytic heterotetramer bound to the RIX^{I} module (*Sp*Rixosome-RIX^{I}-only), with overall dimensions indicated. (**E**) Gold-standard Fourier shell correlation (FSC) curves for the locally refined scaffold (blue, 2.68 Å) and catalytic module (red, 3.01 Å) of the *Sp*Rixosome-RIX^{I}-only reconstruction; dashed line, FSC = 0.143.

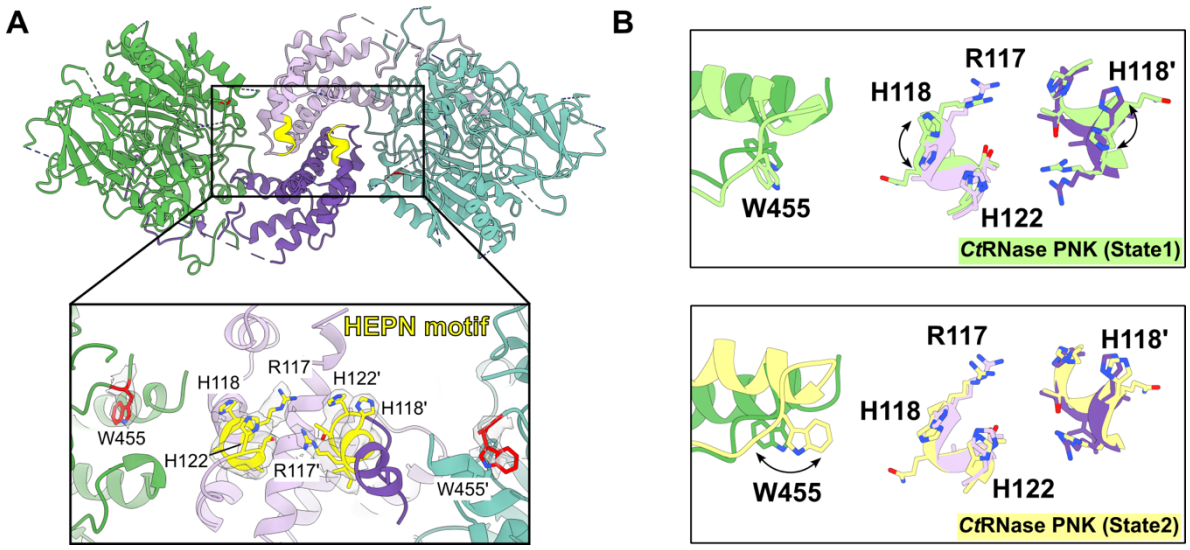

Fig. 2. Structure of the *S. pombe* nuclease–kinase catalytic core. (**A**) Overall structure of the RNase–PNK catalytic heterotetramer (Las1[a], Las1[b], Grc3[a], and Grc3[b]; colored by subunit) within the intact *S. pombe* rixosome. The close-up shows the HEPN active site formed at the Las1[a]–Las1[b] interface; conserved catalytic residues R117, H118, and H122 of each Las1 HEPN protomer, together with the Grc3 W455 clasp, are shown as sticks. Primed labels (for example, R117′) denote the second protomer. (**B**) Superposition of the HEPN active site from the intact rixosome with the previously determined *Chaetomium thermophilum* RNase–PNK structures in the ATP-γS-bound state 1 (top; PDB: 6OF3) and state 2 (bottom; PDB: 6OF2). Curved arrows highlight repositioning of the catalytic histidines and of the W455 clasp relative to the reference states.

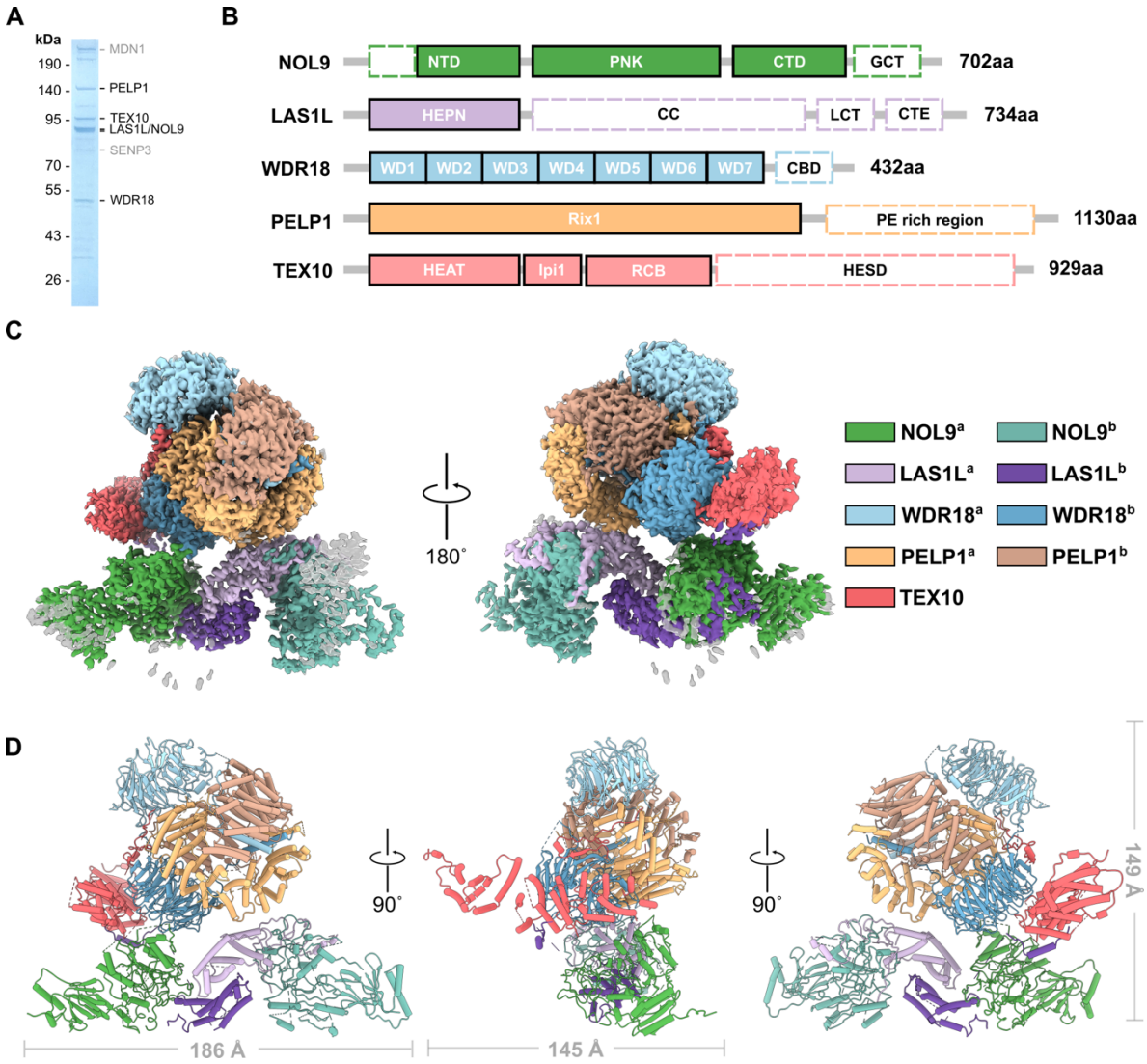

Fig. 3. Cryo-EM structure of the endogenous human rixosome. (**A**) SDS-PAGE analysis of the endogenously purified human rixosome (*Hs*Rixosome), with subunits labeled and identities confirmed by mass spectrometry. (**B**) Domain organization of the *Hs*Rixosome subunits. Dashed outlines indicate regions not resolved in the reconstruction. CTE, C-terminal extension; HESD, higher eukaryote-specific domain; other abbreviations as in Fig. 1B. (**C**) Composite cryo-EM map of the twofold-symmetric RNase–PNK catalytic heterotetramer bound to a single PELP1–TEX10–WDR18 scaffold module, with

subunits color-coded. (**D**) Atomic model of the complex in (C) in three orthogonal views, with overall dimensions indicated.

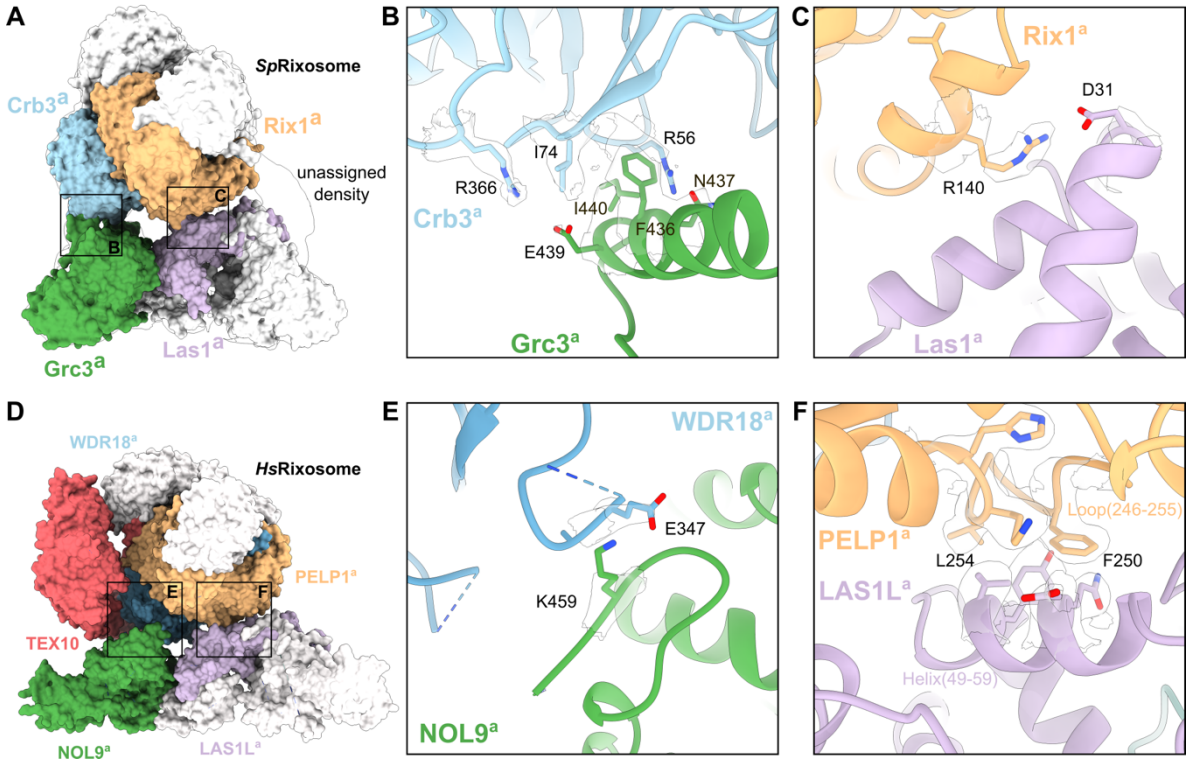

Fig. 4. A conserved mode of rixosome holoenzyme assembly in yeast and human.

(**A**) Overall architecture of the yeast rixosome, with the two scaffold–catalytic core interfaces boxed: the Crb3–Grc3 and Rix1–Las1 interfaces. (**B**) Close-up view of the Crb3–Grc3 interface. Crb3 I74 packs against Grc3 F436 and I440, while Crb3 R56 forms a polar interaction with Grc3 N437. Cryo-EM density is shown for the interacting residues. (**C**) Close-up view of the Rix1–Las1 interface. Rix1 R140 forms a salt bridge with Las1 D31. (**D**) Overall architecture of the human rixosome, with the scaffold–catalytic core interfaces boxed: the WDR18–NOL9 and PELP1–LAS1L interfaces. (**E**) Close-up view of the WDR18–NOL9 interface. WDR18 E347 and NOL9 K459 are positioned to form a salt bridge. (**F**) Close-up view of the PELP1–LAS1L interface. PELP1 F250 and L254 insert into a hydrophobic groove on the HEPN domain of LAS1L, centered on V56.

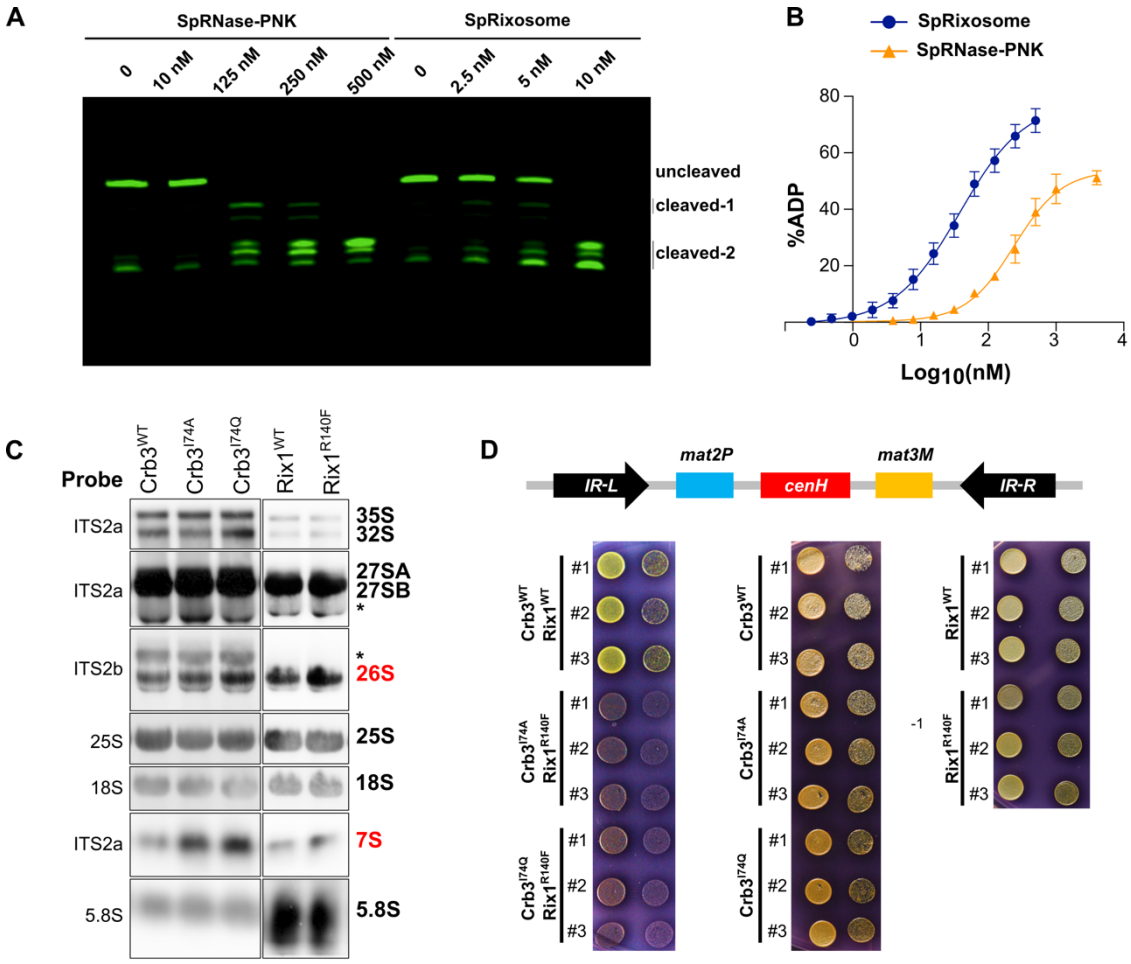

997

998 **Fig. 5. The scaffold module enhances catalytic activity, ITS2 processing, and**

999 **chromatin silencing.** (**A**) In vitro RNA cleavage assay with a 5′-Cy5-labeled 30-nt

1000 SpITS2 fragment. Recombinant *Sp*RNase–PNK and intact *Sp*Rixosome were

1001 compared at the indicated concentrations (0–500 nM and 0–10 nM, respectively).

1002 Uncleaved substrate and the two sequential cleavage products (cleaved-1 and cleaved-

1003 2) are indicated; a representative result from multiple independent experiments is

1004 shown. (**B**) Kinase activity measured by the ADP-Glo assay. ATP-to-ADP conversion

1005 is plotted as a function of protein concentration for recombinant *Sp*RNase–PNK

1006 (orange) and intact *Sp*Rixosome (blue). Error bars, s.d. (n = 3 technical replicates). (**C**)

Northern blot analysis of total RNA from the indicated strains, probed as shown. The 7S pre-rRNA accumulates, accompanied by a modest accumulation of 26S pre-rRNA, in the interface mutants; 35S/32S, 27SA/27SB, 25S, 18S, and 5.8S species are shown for reference. Asterisks denote additional processing intermediates. (**D**) Top, schematic of the *S. pombe* mating-type (*mat*) locus; *mat2P* and *mat3M* are maintained silent by heterochromatin, and derepression triggers mating-type switching and sporulation, detected by iodine staining. Bottom, iodine staining of the indicated strains, with genotypes listed at left (three independent isolates each); dark staining indicates loss of silencing. The assay is assessed qualitatively.

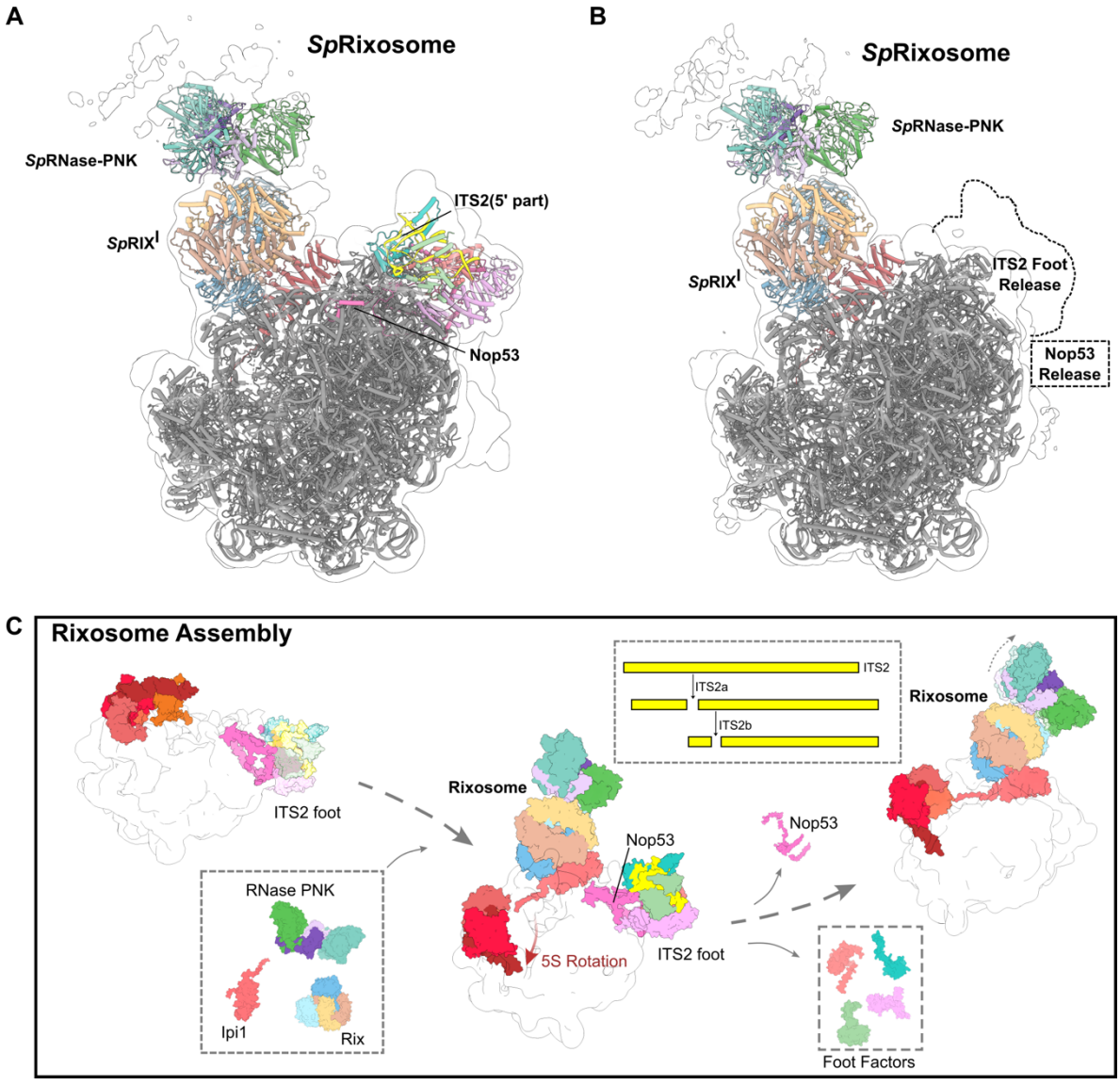

Fig. 6. Native rixosome-bound pre-60S intermediates define the order of ITS2-foot processing and rixosome release. (**A**) Rixosome-bound pre-60S particle with an intact ITS2 foot. The RIX scaffold (*Sp*RIX^{I}) is stably anchored at the ITS2 foot, density for the ITS2 5′ region is visible, and Nop53 is bound at the base of the foot; the RNase–PNK catalytic core and the second RIX scaffold module (*Sp*RIX^{II}) remain conformationally flexible. (**B**) Rixosome-bound pre-60S particle after ITS2-foot release. Neither the ITS2 foot nor Nop53 is detectable (dashed outlines), yet the RIX scaffold remains bound at the

same site, showing that rixosome release is not coupled to removal of the ITS2 foot. (**C**) Model for rixosome action during 5S RNP rotation and ITS2 processing; the ITS2 foot is processed while the rixosome remains bound, followed by release of foot-associated factors and subsequent rixosome disengagement.

Supplementary Information

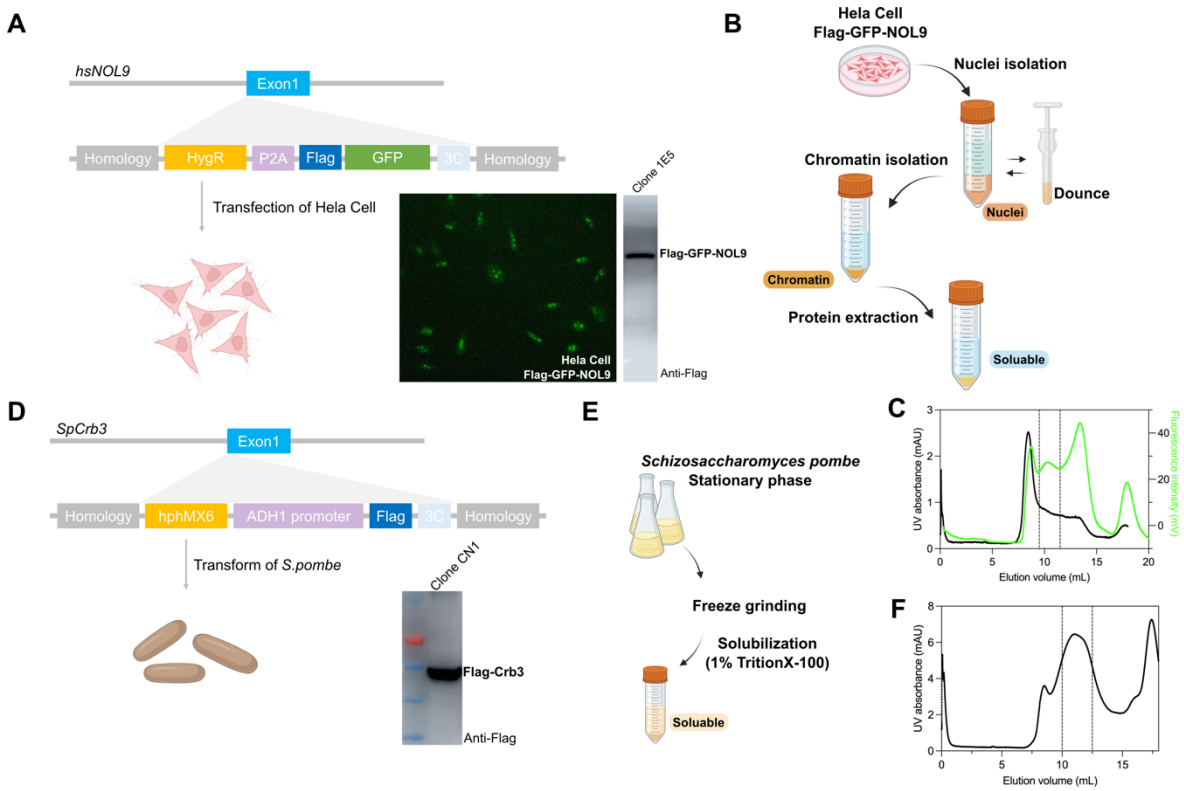

Fig. S1. Endogenous tagging and purification of human and *S. pombe* rixosome complexes. (**A**) Top: CRISPR-Cas9 knock-in strategy for HeLa Flag-GFP-NOL9 cells. Bottom: fluorescence microscopy and anti-Flag immunoblot of a representative clone. (**B**) Purification workflow for endogenous *Hs*Rixosome: nuclear isolation, chromatin extraction, soluble fraction followed by anti-Flag affinity purification, and size-exclusion chromatography (SEC). (**C**) *S. pombe* Flag-Crb3 tagging strategy. Anti-Flag immunoblot confirms expression from the endogenous locus. (**D**) Purification workflow for endogenous *Sp*Rixosome: cryogenic milling of stationary-phase cells, solubilization in 1% Triton X-100, affinity purification, and SEC. (**E**) SEC profile of *Hs*Rixosome monitored by A_{280} and GFP fluorescence. (**F**) SEC profile of *Sp*Rixosome monitored by A_{280}. The major peak corresponds to the intact holoenzyme.

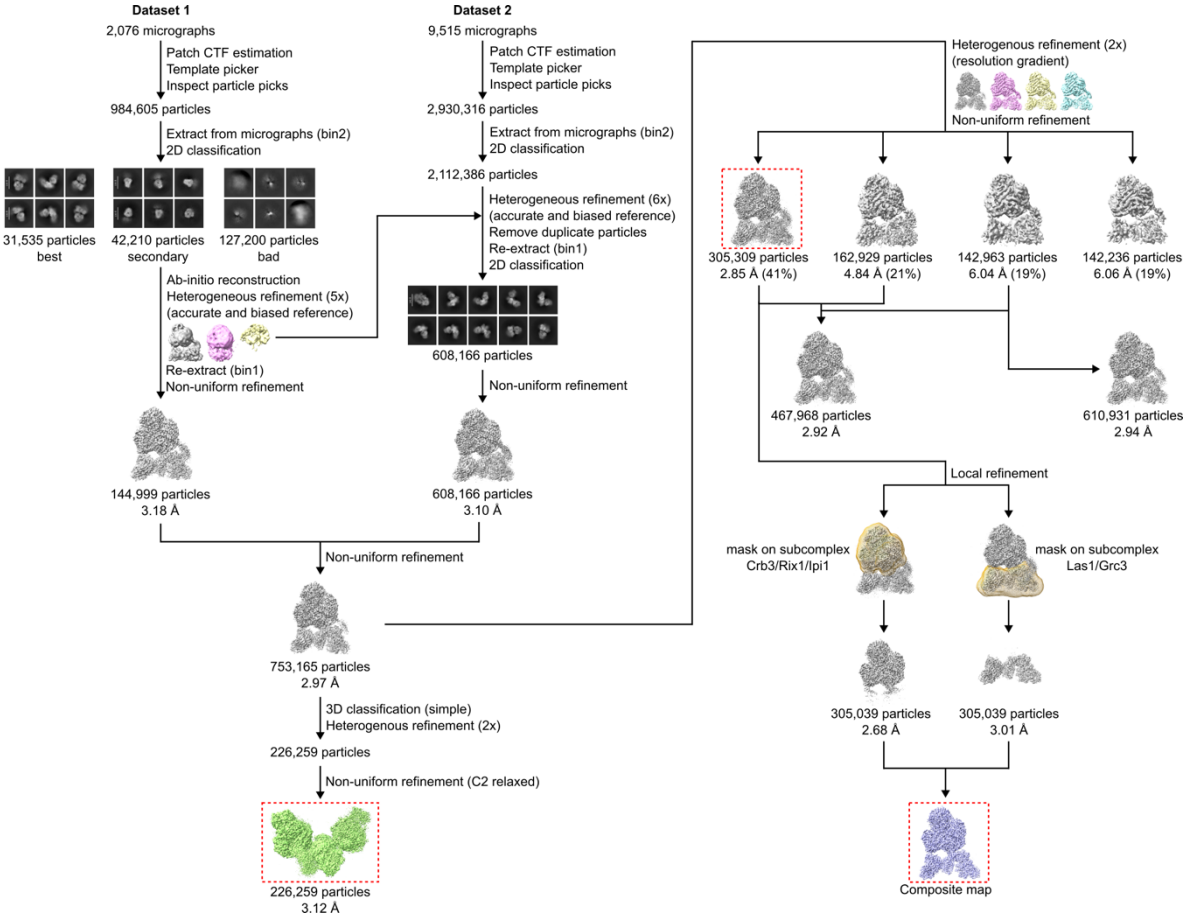

Fig. S2. Cryo-EM data processing for the *S. pombe* rixosome. Processing flowchart. Two datasets (2,076 and 9,515 micrographs) were collected. After 2D classification and 3D refinement with relaxed C2 symmetry, a consensus reconstruction reached 2.97 Å. Three-dimensional classification separated the two-module assembly (2,226,259 particles; 3.12 Å after non-uniform refinement with relaxed C2 symmetry) from the predominant single-module species (305,039 particles; 2.85 Å). Focused local refinement of the RIX^{I} scaffold (Crb3–Rix1–Ipi1) and the RNase–PNK catalytic module (Las1–Grc3) within this species yielded maps at 2.68 and 3.01 Å, respectively, which were combined into the composite map used for model building (*Sp*Rixosome-RIX^{I}-only). Processing was performed in cryoSPARC; see Methods for parameters.

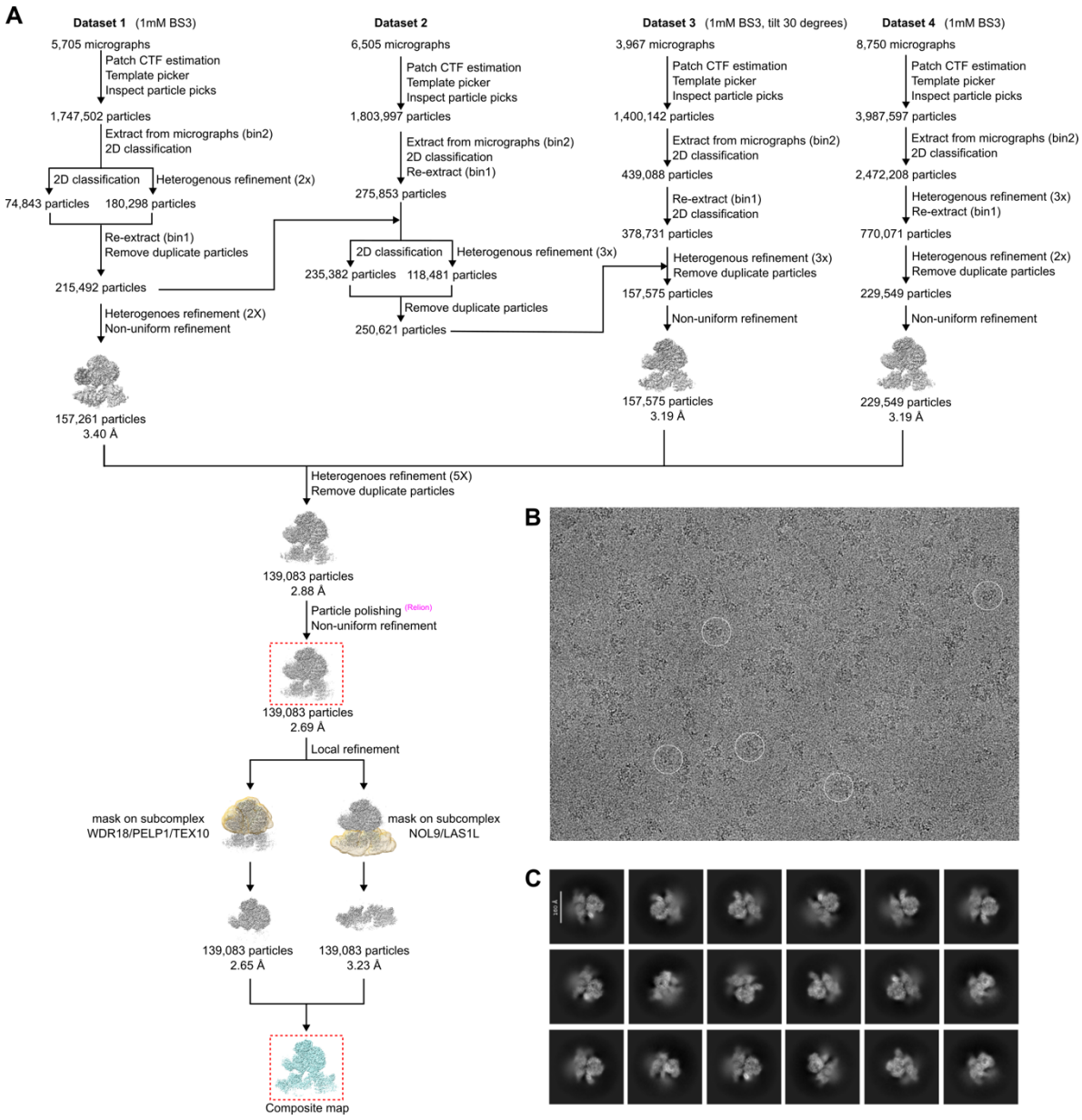

Fig. S3. Cryo-EM data processing for the human rixosome. (**A**) Processing flowchart. Four datasets (5,705; 6,505; 3,967; 8,750 micrographs; dataset 3 collected with a 30° tilt) were combined. Heterogeneous refinement, Bayesian polishing, and non-uniform refinement yielded a consensus reconstruction at 2.69 Å. Local refinement of the scaffold (WDR18–PELP1–TEX10) and catalytic (NOL9–LAS1L) modules produced maps at 2.65 and 3.23 Å, respectively. Processing was performed in cryoSPARC and RELION; see

Methods for parameters. (**B**) Representative raw micrograph. Selected particles are circled. (**C**) Reference-free 2D class averages.

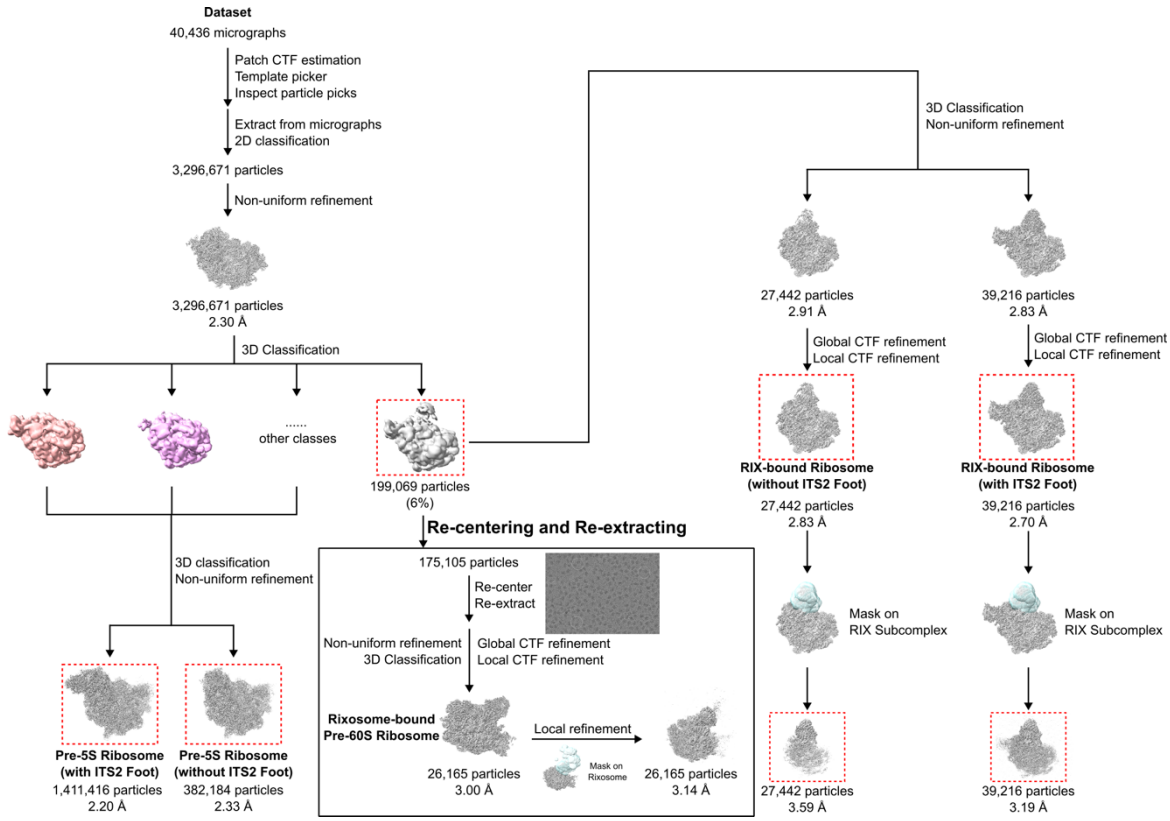

Fig. S4. Cryo-EM data processing for the *S. pombe* pre-60S particles. Flowchart of cryo-EM data processing. A dataset of 40,436 micrographs yielded 3,296,671 particles after automated particle picking and reference-free 2D classification, and non-uniform refinement produced an initial consensus reconstruction at 2.30 Å. Three-dimensional classification resolved two major classes corresponding to the Pre-5S rotation pre-60S ribosome with (1,411,416 particles, 2.20 Å) and without (382,184 particles, 2.33 Å) the ITS2 foot, together with a minor particle subset carrying rixosome density (199,069 particles, ~6%) and other classes. Within the minor subset, 3D classification and non-uniform refinement yielded two RIX-bound ribosome states, with (39,216 particles, 2.70 Å) and without (27,442 particles, 2.83 Å) the ITS2 foot; global and local CTF refinement followed by masked local refinement of the RIX region gave maps at 3.19 Å and 3.59 Å,

respectively. In parallel, the minor subset was re-centered and re-extracted (175,105 particles), and further 3D classification yielded a class containing a relatively stable rixosome (26,165 particles, 3.00 Å) that improved to 3.14 Å after masked local refinement on intact rixosome. Image processing was performed in cryoSPARC; see Methods for details.

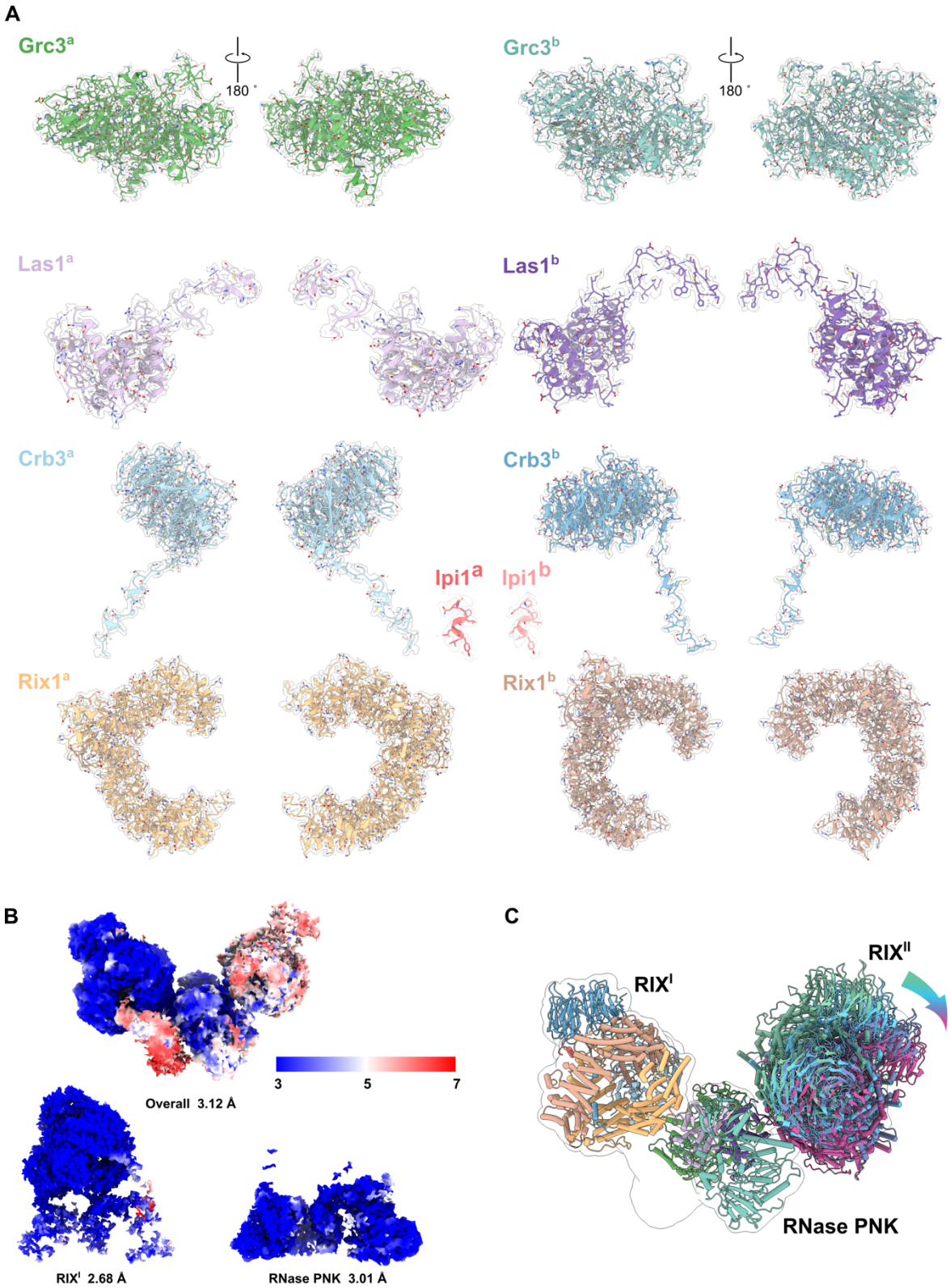

1082

Fig. S5. Cryo-EM density, local resolution, and conformational variability of the SpRixosome-RIX^{I}-only. (**A**) Density for individual subunits (Grc3$^{a/b}$, Las1$^{a/b}$, Crb3$^{a/b}$, Rix1$^{a/b}$, Ipi1$^{a/b}$) with fitted atomic models shown in two orthogonal views related by a 180° rotation. (**B**) Local-resolution maps of the overall SpRixosome reconstruction (3.12 Å) and of the locally refined scaffold (2.68 Å) and RNase–PNK catalytic module (3.01 Å) of the SpRixosome-RIX^{I}-only species, colored by local resolution (3–7 Å, as indicated). (**C**) Structural superposition of RIX^{I} (solid colors) and RIX^{II} (colored according to conformational variability), illustrating the ~30° conformational swing of the flexible module.

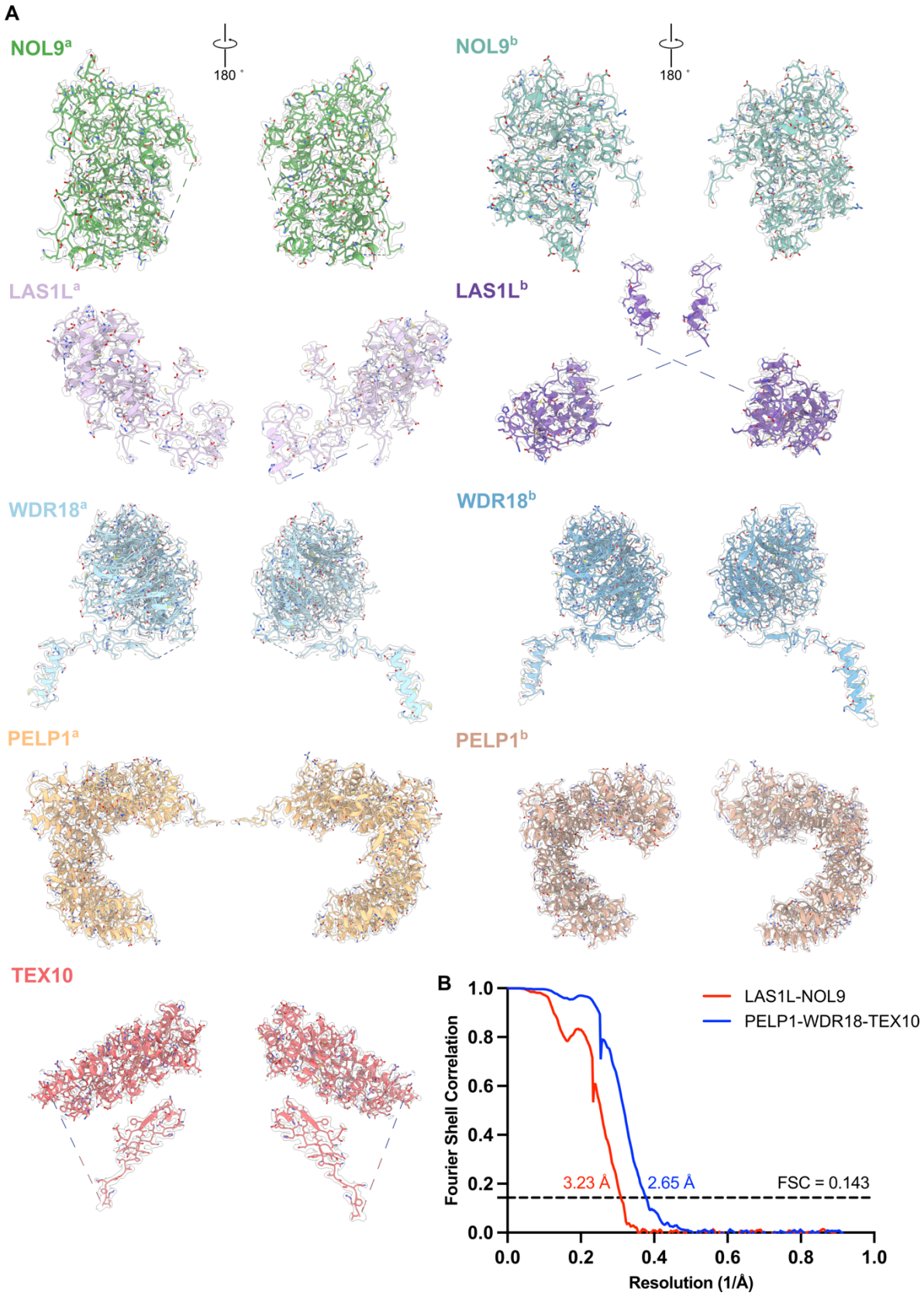

1092

Fig. S6. Cryo-EM density and map–model agreement for the *Hs*Rixosome. (**A**) Density for individual subunits (NOL9[a/b], LAS1L[a/b], WDR18[a/b], PELP1[a/b], TEX10) with fitted atomic models shown in two orthogonal views related by a 180° rotation. (**B**) Gold-standard FSC curves for locally refined *Hs*Rixosome scaffold (blue, 2.65 Å) and catalytic module (red, 3.23 Å). Dashed line, FSC = 0.143.

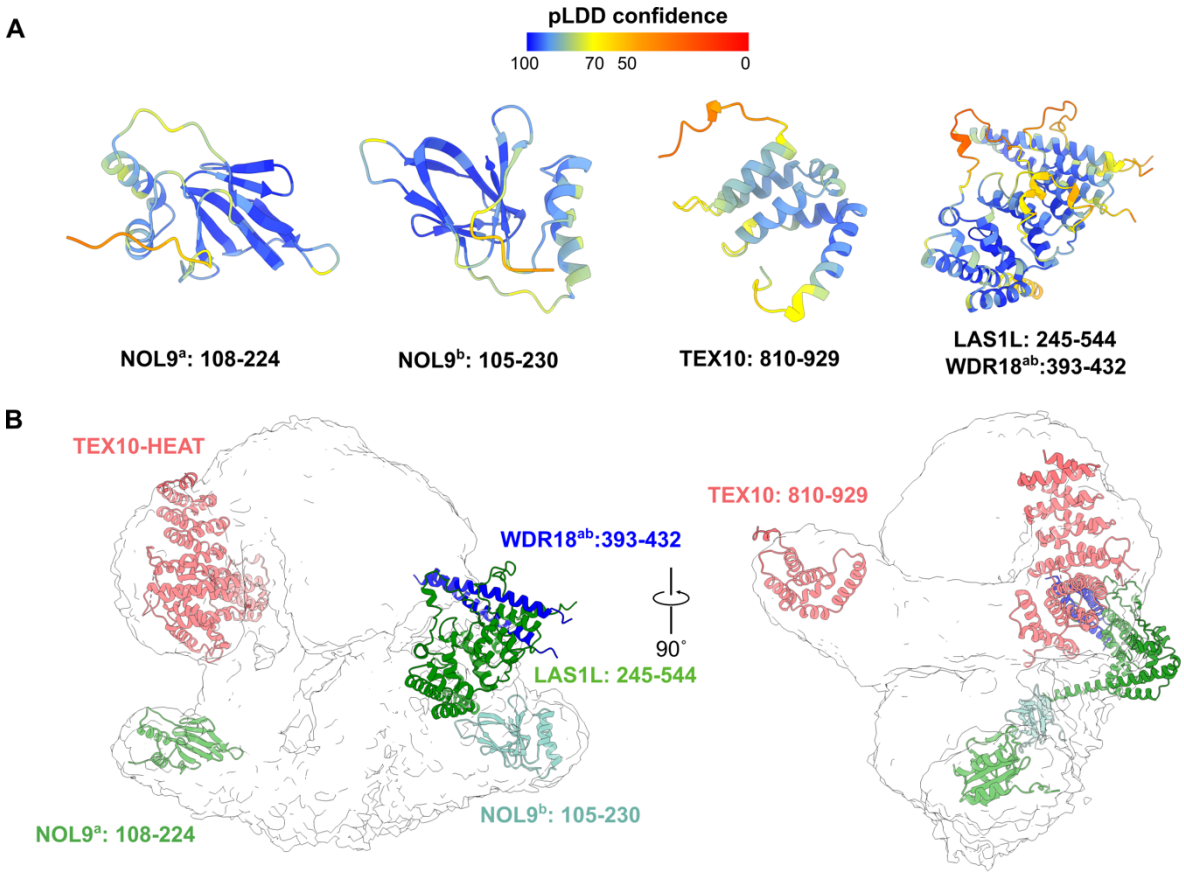

Fig. S7. AlphaFold3-predicted models docked into the *Hs*Rixosome cryo-EM map. (**A**) AlphaFold3 predictions for regions unresolved at high resolution: NOL9$^{a/b}$ CTDs, the N-terminal region of TEX10, and LAS1L coiled-coil–WDR18 CBD interaction. Colored by pLDDT confidence (blue, high; red, low). (**B**) Rigid-body docking into a low-pass-filtered (6 Å) *Hs*Rixosome map. The TEX10 HEAT domain fit is based on PDB: 8PV2.

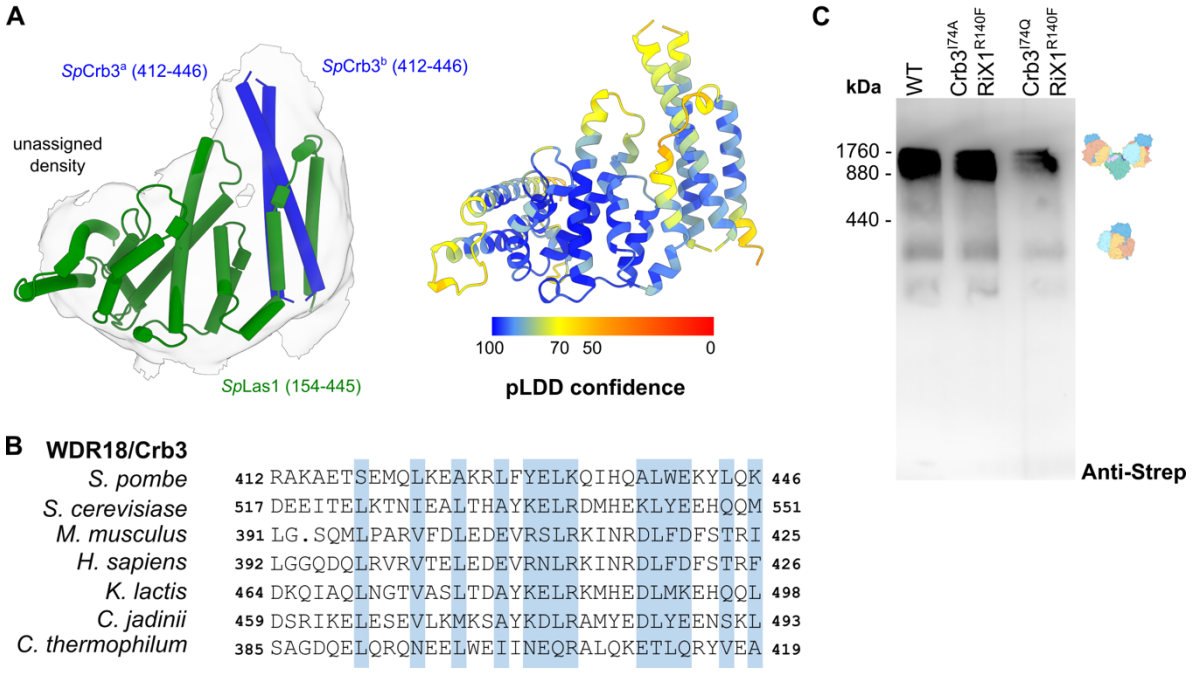

Fig. S8. Conserved scaffold–core interfaces and rixosome integrity. (**A**) Predicted Crb3–Las1 coiled-coil interaction. Left: A low-pass-filtered cryo-EM map of the Crb3 C-terminal segment and Las1 coiled-coil is shown. The structural model of the Crb3 C-terminal segment (residues 412–446) and Las1 coiled-coil domain (residues 154–445) predicted by AlphaFold3 was rigid-body docked into the low-pass-filtered map. Right: The AlphaFold3-predicted complex model of the Crb3 C-terminal segment and Las1 coiled-coil domain is colored by the pLDDT confidence score. (**B**) Multiple sequence alignment of the CBD region of WDR18/Crb3 orthologs. Conserved residues are highlighted. (**C**) Native PAGE results of wild-type and interface-mutant *Sp*Rixosomes. Wild-type and interface-mutants of *Sp*Rixosomes were subjected to native PAGE gel and imaged by anti-Strep western blotting. Representative particle species are depicted.

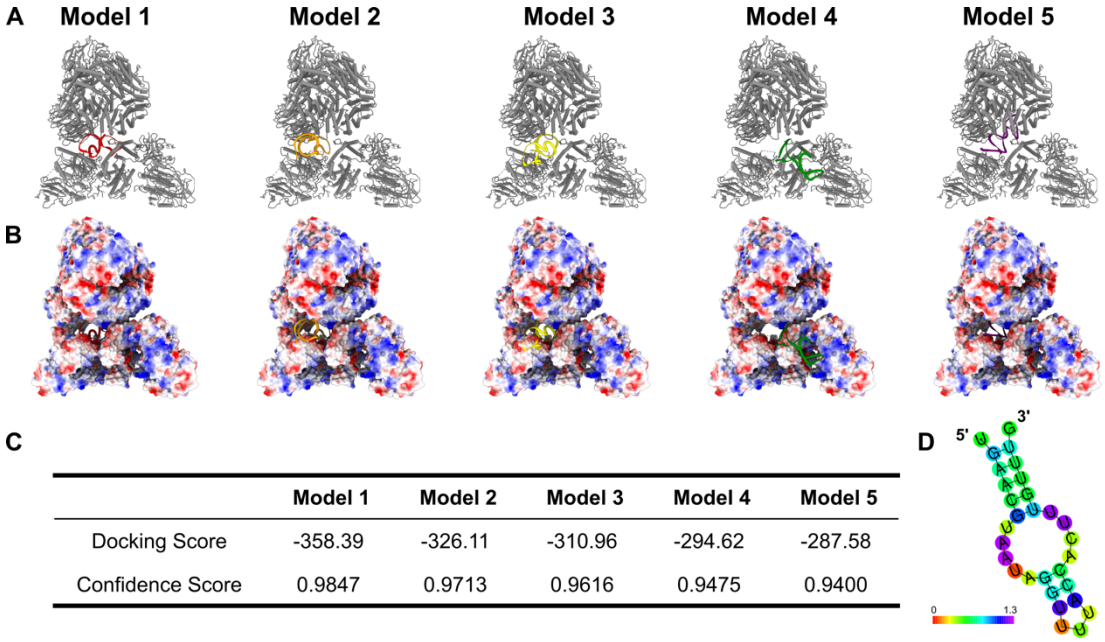

	Model 1	Model 2	Model 3	Model 4	Model 5
Docking Score	-358.39	-326.11	-310.96	-294.62	-287.58
Confidence Score	0.9847	0.9713	0.9616	0.9475	0.9400

Fig. S9. HDOCK prediction of ITS2 RNA docking onto the *Sp*Rixosome. (**A**) Top five HDOCK models for a 30-nt ITS2-derived RNA fragment docked onto the *Sp*Rixosome. RNA is shown in cartoon representation. (**B**) Electrostatic surface potential (blue, positive; red, negative). Docked RNA preferentially occupies an electropositive channel at the scaffold–core junction. (**C**) Docking and confidence scores for the five highest-ranked models. (**D**) Sequence and secondary structure of the docking substrate, corresponding to the region flanking the C2 cleavage site within *Sp*ITS2.

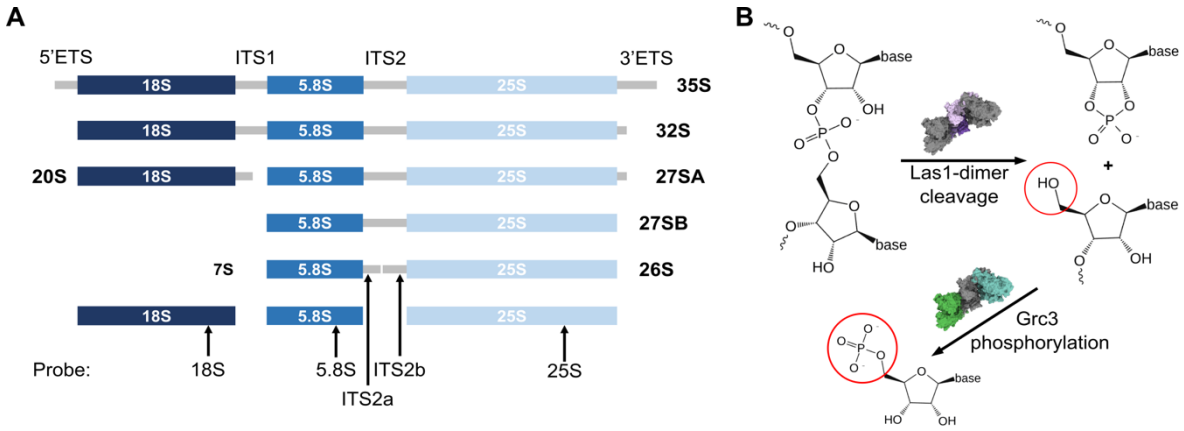

Fig. S10. Pre-rRNA processing pathway and ITS2 cleavage in *S. pombe*. (**A**) Schematic of the *S. pombe* pre-rRNA processing pathway. The 35S primary transcript and the 32S, 27SA, 27SB, 26S and 7S processing intermediates are shown; arrows indicate the binding sites of the 18S, 5.8S, ITS2a, ITS2b and 25S probes used for northern blotting. The ITS2a and ITS2b probes flank the C2 cleavage site and monitor processing of the ITS2 region, whereas the 18S, 5.8S, and 25S probes detect rRNA-containing precursors and mature rRNAs. (**B**) The coupled nuclease–kinase mechanism. Las1 cleaves ITS2 to generate a 5′-OH terminus and a 2′,3′-cyclic phosphate, and Grc3 subsequently phosphorylates this end to produce a 5′-phosphate, marking the 7S pre-rRNA for exosome-mediated 3′→5′ degradation.

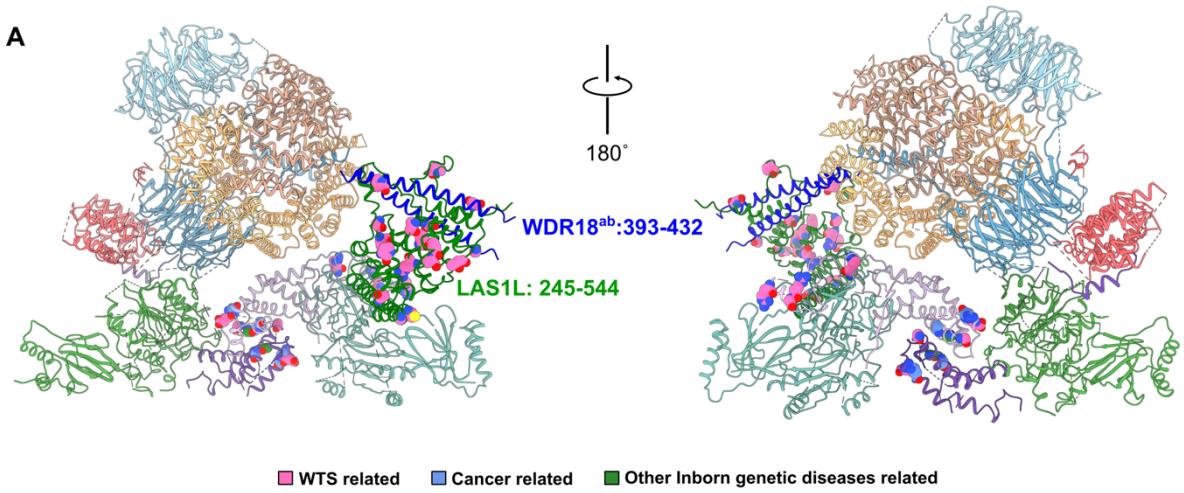

B

Disease-associated mutation in the structure-resolved LAS1L

Position(s)	Change	Description	Clinical significance
107	G>D	WTS	VUS
116	G>A	Inborn genetic diseases	VUS
118	A>V	Thyroid cancer, nonmedullary	VUS
168	D>N	WTS	VUS
170	R>C	a colorectal cancer sample; somatic mutation	VUS
624	R>K	WTS	VUS
630	R>I	WTS	VUS
654	R>L	WTS	VUS

WTS: Wilson-Turner syndrome

VUS: Variant of uncertain significance

Disease-associated mutation in LAS1L CC domain

Position(s)	Change	Description	Clinical significance
269	**A>G**	**WTS**	**Pathogenic**
313	G>S	WTS	VUS
316	C>Y	WTS	Likely benign
361	P>R	WTS	Likely benign
372	V>I	WTS	Benign
377	P>A	WTS	VUS
401	R>S	WTS	VUS
413	G>R	WTS	Likely pathogenic
415	**R>W**	**WTS**	**Pathogenic**
424	V>I	WTS	VUS
428	V>M	WTS	VUS
429	A>T	WTS	VUS
433	T>I	WTS	VUS
477	S>N	WTS	Likely pathogenic
491	G>D	WTS	VUS
524	P>A/H/T	WTS	VUS

Fig. S11. Disease-associated LAS1L variants mapped onto the human rixosome. **(A)** Ribbon representation of the intact human holoenzyme in two orthogonal views. Disease-associated residues are colored by condition: pink, Wilson–Turner syndrome; blue, cancer; green, other inborn genetic diseases. **(B)** Table of disease-associated LAS1L variants. The variants cluster in the HEPN and coiled-coil (CC) domains of LAS1L.

Table S1 | Statistics for data collection and structural modeling of the *Sp*Rixosome-RIX^{I}-only reconstruction.

	***Sp*Rixosome-RIX^{I}-only**	**RIX^{I}**	**RNase-PNK**
Data collection			
EM equipment	Titan Krios G3i (Thermo Fisher Scientific Inc.)		
Voltage (kV)	300		
Detector	Gatan K3 Summit		
Energy filter	Gatan GIF Quantum, 20 eV slit		
Pixel size (Å)	1.087		
Electron dose (e^-/Å^2)	50		
Defocus range (μm)	−1.4 ~ −2.0		
Number of collected movie stacks	11,591		
Reconstruction			
Software	CryoSPARC v4		
Number of used particles	305,039	305,039	305,039
Symmetry	C1	C1	C1
Resolution (Å)	2.85	2.68	3.01
Map sharpening B-factor (Å^2)	110.9	105.1	114.4
Refinement			
Software	Phenix		
Model composition			
Non-hydrogen atoms	24,597	14,129	10,468
Protein residues	3,125	1,806	1,319
Ligands	0	0	0
R.m.s deviations			
Bonds length (Å)	0.005	0.005	0.004
Bonds angle (°)	0.989	1.010	0.960
MolProbity score	1.80	1.68	1.92
Clashscore	4.24	3.74	4.86
Ramachandran plot statistics (%)			
Preferred	97.21%	97.75%	96.45%
Allowed	2.76%	2.19%	3.55%
Outlier	0.03 %	0.06%	0.00%

1149 **Table S2 | Statistics for data collection and structural modeling of the human rixosome.**

	***Hs*Rixosome**	**Scaffold**	**RNase-PNK**
Data collection			
EM equipment	Titan Krios G3i (Thermo Fisher Scientific Inc.)		
Voltage (kV)	300		
Detector	Gatan K3 Summit		
Energy filter	Gatan GIF Quantum, 20 eV slit		
Pixel size (Å)	1.087		
Electron dose (e^-/Å^2)	50		
Defocus range (μm)	−1.4 ~ −2.0		
Number of collected movie stacks	24,927		
Reconstruction			
Software	CryoSPARC v4		
Number of used particles	139,083	139,083	139,083
Symmetry	C1	C1	C1
Resolution (Å)	2.69	2.65	3.23
Map sharpening B-factor (Å^2)	62.5	60.4	66.0
Refinement			
Software	Phenix		
Model composition			
Non-hydrogen atoms	22,609	15,470	7,139
Protein residues	2,931	2,031	900
Ligands	0	0	0
R.m.s deviations			
Bonds length (Å)	0.004	0.004	0.004
Bonds angle (°)	0.972	0.955	1.008
MolProbity score	1.93	1.50	2.45
Clashscore	5.11	3.33	8.77
Ramachandran plot statistics (%)			
Preferred	95.49%	97.75%	90.57%
Allowed	4.44%	2.33%	9.43%
Outlier	0.07%	0.10%	0.00%

1150

Table S3 | Statistics for data collection and structural modeling of the *S. pombe* Pre-5S rotation pre-60S ribosome: global reconstruction and local refinement of the 5S rotation-associated factors.

	Pre-5S rotation Pre-60S ribosome (no ITS2 Foot)		Pre-5S rotation Pre-60S ribosome (with ITS2 Foot)	
	Global	**Local**	**Global**	**Local**
Data collection				
EM equipment	Titan Krios G3i (Thermo Fisher Scientific Inc.)			
Voltage (kV)	300			
Detector	Gatan K3 Summit			
Energy filter	Gatan GIF Quantum, 20 eV slit			
Pixel size (Å)	1.087			
Electron dose (e^-/Å^2)	50			
Defocus range (μm)	−1.4 ~ −2.0			
Number of collected movie stacks	40,436			
Reconstruction				
Software	CryoSPARC v4			
Number of used particles	382,184		1,411,416	
Symmetry	C1		C1	
Resolution (Å)	2.33	2.60	2.20	2.31
Map sharpening B-factor (Å^2)	57.8	67.7	63.7	66.5
Refinement				
Software	Phenix			
Model composition				
Non-hydrogen atoms	102,790	11,354	113,771	11,354
Protein residues	6,660	1,126	7,809	1,126
Nucleotide	2,421	109	2,498	109
Ligands	Zn: 1	0	Zn: 1	0
R.m.s deviations				
Bonds length (Å)	0.005	0.004	0.005	0.003
Bonds angle (°)	0.917	0.907	0.995	0.887
MolProbity score	1.63	1.76	1.62	1.37
Clashscore	2.57	4.07	2.94	2.64
Ramachandran plot statistics (%)				
Preferred	95.96%	97.03%	96.17%	97.93%
Allowed	4.04%	2.97%	3.77%	2.07%
Outlier	0.00%	0.00%	0.05%	0.00%

Table S4 | Statistics for data collection and structural modeling of the *S. pombe* rixosome-bound pre-60S ribosome: global reconstruction and local refinement of the RIX[1] subcomplex.

	Rixosome-bound pre-60S ribosome (no ITS2 Foot)		Rixosome-bound pre-60S ribosome (with ITS2 Foot)	
	Global	**Local**	**Global**	**Local**
Data collection				
EM equipment	Titan Krios G3i (Thermo Fisher Scientific Inc.)			
Voltage (kV)	300			
Detector	Gatan K3 Summit			
Energy filter	Gatan GIF Quantum, 20 eV slit			
Pixel size (Å)	1.087			
Electron dose (e^-/Å^2)	50			
Defocus range (μm)	−1.4 ~ −2.0			
Number of collected movie stacks	40,436			
Reconstruction				
Software	CryoSPARC v4			
Number of used particles	27,442		39,216	
Symmetry	C1		C1	
Resolution (Å)	2.83	3.59	2.70	3.19
Map sharpening B-factor (Å^2)	34.1	48.5	38.3	48.2
Refinement				
Software	Phenix			
Model composition				
Non-hydrogen atoms	127,171	14,063	137,260	14,063
Protein residues	8,556	1,798	9,659	1,798
Nucleotide	2,856	0	2,907	0
Ligands	Zn: 1	0	Zn: 1	0
R.m.s deviations				
Bonds length (Å)	0.005	0.004	0.006	0.005
Bonds angle (°)	0.844	1.034	0.863	1.004
MolProbity score	1.82	2.06	1.75	1.94
Clashscore	3.84	8.04	3.67	5.83
Ramachandran plot statistics (%)				
Preferred	95.25%	97.01%	95.68%	95.99%
Allowed	4.71%	2.88%	4.27%	4.01%
Outlier	0.04%	0.11%	0.05%	0.00%